Tunnelling and Underground Space Technology 144 (2024) 105537

Contents lists available at ScienceDirect

Tunnelling and Underground Space Technology incorporating Trenchless Technology Research

journal homepage: www.elsevier.com/locate/tust

Effects of anisotropic shale creep on the stress and permeability evolution of a geological nuclear waste repository

Tsubasa Sasaki *, Jonny Rutqvist

Earth Sciences Division, Lawrence Berkeley National Laboratory, 1 Cyclotron Road, Berkeley, CA 94720, USA

ARTICLE INFO

Keywords:
Anisotropic
Shale
Creep
Nuclear waste
Repository
Coupled processes

ABSTRACT

To ensure long-term safety and performance, geological nuclear waste repositories require low-permeability barriers such as bentonite buffers and/or shale host rock. Shale is not only known for its low permeability but also for its trend to undergo time-dependent deformation (i.e., creep), which could heal damage, but the effects of shale creep on the long-term performance of nuclear waste repositories have not been clearly understood. In particular, the anisotropic nature of shale (i.e., bedding) could have a significant effect on its creep behavior, and consequently, on the long-term performance of nuclear waste repositories. In this research, numerical simulations were carried out with the objective of showing the effects of anisotropic shale creep on the stress and permeability evolution of a generic geological nuclear waste repository in shale. The TOUGH-FLAC simulator, a thermo-hydromechanically (THM) coupled numerical code, was used for the simulations. To achieve the objective, comparisons were performed between the results of anisotropic shale creep simulations and those of different simulation cases, namely, no creep (i.e., elastic), isotropic creep, and long-term creep shale cases. Results of the comparisons show that the elastic and isotropic creep shale cases respectively led to the overestimation and underestimation of stress and permeability in the repository, whereas the long-term creep shale case, which accumulated greater creep in later periods than in earlier periods, helped to keep large shear and tensile stresses from developing while maintaining compressive spherical stress, resulting in consistently low permeability levels. These results indicate that performance assessments with elastic and isotropic creep formation models will provide the upper and lower bound estimates of stress and permeability, while more reasonable estimates will be given by an anisotropic creep formation model, and that shale with long-term creep characteristics will be beneficial in many aspects of the safety and performance of nuclear waste repositories.

1. Introduction

Geological nuclear waste repositories have been proposed as a permanent solution for storing and disposing of high-level radioactive waste and spent fuel (IAEA, 2003). It is designed to isolate high-level radioactive waste from the biosphere with a multi-barrier system (Apted and Ahn, 2010). The barrier system comprises a natural barrier (i.e., bedrock) and an engineered barrier system (EBS); the former provides secondary protection as low-permeability formations impedes the transport of radionuclides if they are released, and the latter is the primary protection in which compacted clay (e.g., bentonite) that fills the gap between the waste packages emplaced in subsurface drifts and the surrounding formation provides hydromechanical stability for both the waste packages and the formation.

A potential issue about the multi-barrier system is the development of the excavation damaged zone (EDZ) in the formation around waste emplacement drifts. As the EDZ is typically highly fractured, it could provide pathways for the transport of radionuclides if they are released from the waste packages (Tsang et al., 2005). The behavior of the EDZ and the surrounding formation is strongly thermo-hydromechanically (THM) coupled (Tsang, 1987), which could not only induce further damage but also some healing in the EDZ, in which case the permeability recovers toward that of an intact formation with time (Blümling et al., 2007).

Coupled processes associated with geological nuclear waste repositories have been studied at underground research laboratories (URL) (Bechthold et al., 1999; Bossart et al., 2002; Conil et al., 2020; Thomas et al., 2014; Yu et al., 2014). Results from URLs have been utilized in numerical modelling, which indicates the potential failure of the EDZ and EBS (Rutqvist, 2020; Rutqvist et al., 2014; Sasaki and

* Corresponding author.
E-mail address: tsubasasasaki@lbl.gov (T. Sasaki).

https://doi.org/10.1016/j.tust.2023.105537
Received 29 August 2023; Received in revised form 28 October 2023; Accepted 5 December 2023
Available online 12 December 2023

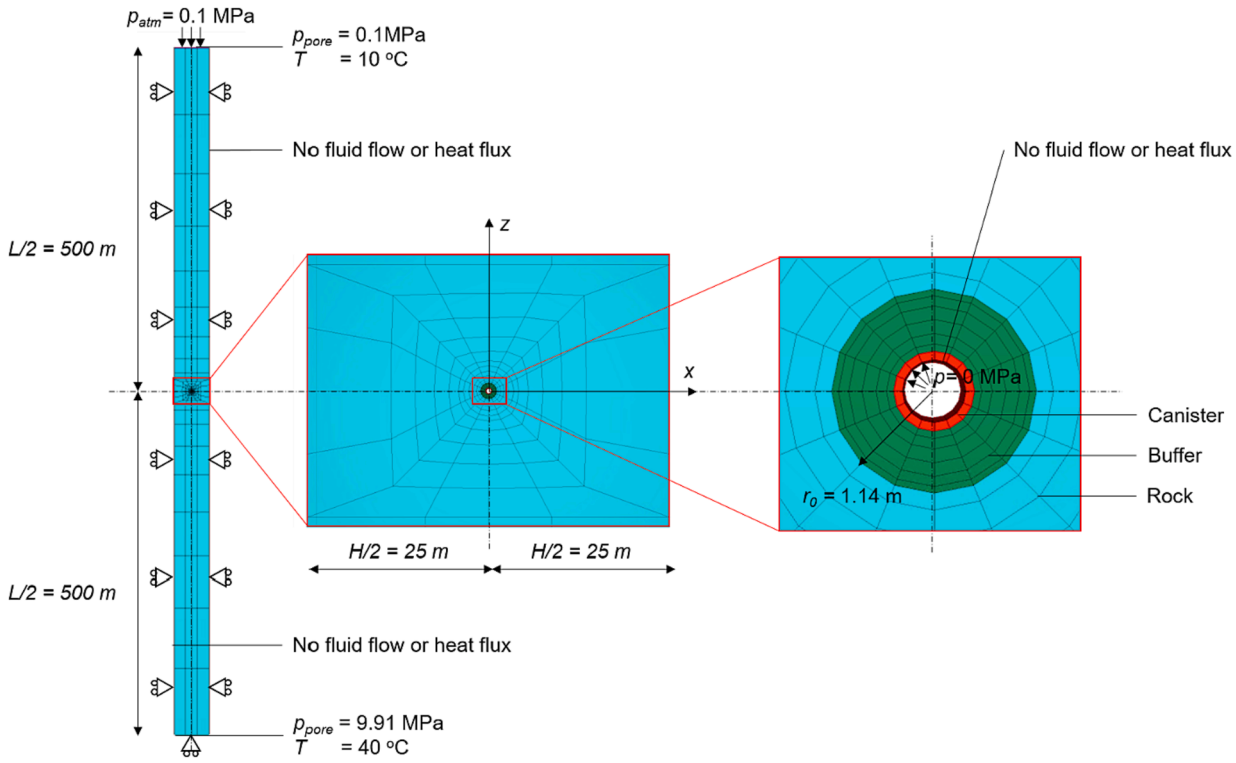

Fig. 1. The geometry, components, and boundary conditions of the repository model.

Table 1
The thermo-hydrological parameters of the nuclear waste repository model.

	Rock	Buffer	Canister
Grain density (kg/m^3)	2700	2700	7800
Porosity (-)	0.15	0.41	0.001
Absolute permeability (//) (m^2)	5 E-20	2 E-21	2 E-21
Absolute permeability (⊥) (m^2)	2 E-20	2 E-21	2 E-21
Thermal conductivity (//) (W/(m·°C))	2.2	1.26	12.0
Thermal conductivity (⊥) (W/(m·°C))	1.4	1.26	12.0
Grain specific heat (J/(kg·°C))	900	800	500
Linear thermal expansivity coefficient (1/°C)	45 E-6	100 E-6	0
Diffusion coefficient for water vapor (m^2/s)	1.73E-5	1.73 E-5	1.73 E-5
van Genuchten parameter, λ_k (-)	0.41	0.32	0.32
Residual liquid saturation for relative permeability, S_{lr} (-)	0.2	–	–
Residual liquid saturation for capillary pressure, S_{lr} (-)	0.1	0.1	0.1
Saturated liquid saturation, S_{ls} (-)	1.0	1.0	1
Residual gas saturation, S_{gr} (-)	0.01	0	0
Capillary pressure parameter, P_0 (Pa)	4.76E7	3E7	3E7
Maximum capillary pressure, P_{max} (Pa)	1E8	5E9	5E9

Table 2
The mechanical parameters of the canister and bentonite buffer.

	Buffer	Canister
Young's modulus (GPa)	20E-3	200
Poisson's ratio (-)	0.35	0.30
Swelling coefficient (-)	0.238	N/A

Rutqvist, 2021). The main causes of EDZ damage are stress changes during not only excavation but also the post-closure period where thermal pressurization and thermal stress development occur. Thermal pressurization causes pore pressure buildup owing to the thermal expansion of pore fluids being greater than that of rocks, whereas thermal stress is due to the thermal expansion of rocks under mechanical

Table 3
The parameters and their values of the permeability function.

Parameter	Value
Residual permeability (//), k_r (m^2)	5E-20
Residual permeability (⊥), k_r (m^2)	2E-20
Permeability increment, $\triangle k_{max}$ (m^2)	1E-17
Mean effective stress parameter, β_1 (1/MPa)	−1
Deviatoric stress parameter, γ(1/MPa)	0.3
Critical deviatoric stress, $\sigma_{d,\ crit}$ (MPa)	5

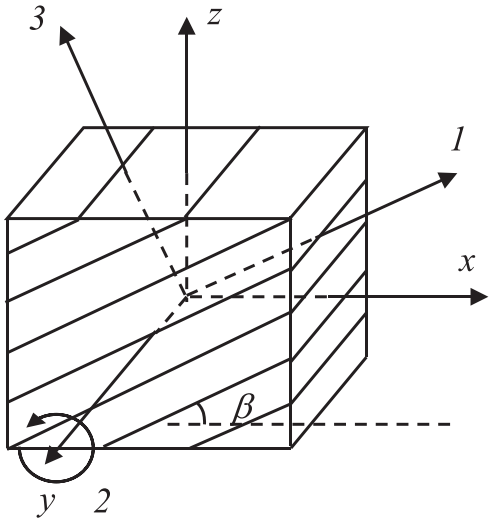

Fig. 2. The global and local coordinates defined with respect to the bedding of shale.

Table 4
The mechanical properties and their values of the Haynesville-1 V and Barnett-1H shales.

	Haynesville-1 V	Barnett-1H
Young's modulus (//) E_P* (GPa)	40	40
Young's modulus (⊥) E_N* (GPa)	20	20
Poisson's ratio (//) ν_P* (-)	0.3	0.3
Poisson's ratio (⊥) ν_N* (-)	0.2	0.2
Shear modulus (⊥) G_N (GPa)	8.3	8.3
c_V (-)	1	1
c_H (-)	0.4	0.8
c_S (-)	1	1
n (-)	1	1
m (-)	0.16	0.16
A (s^{-1})	4.9E-12	1.1E-12
e_{shift} (-)	1E-6	1E-6
σ_{ref} (-)	1	1
t_{ref} (-)	1	1
M** (-)	0.8	1.5
p_0 (MPa)	30	20
ϕ* (%)	6	6
$(\lambda - \kappa) \approx \lambda$*** (-)	0.01	0.01

* (Sone & Zoback, 2013a).
** (Sone & Zoback, 2013b).
*** (Miranda et al., 2020).

confinement (e.g., limited lateral displacement in deep subsurface formations). Thermal stress, for example, could concentrate near waste emplacement drifts (Rutqvist, 2020), leading to further damage in the EDZ.

Although damage in the EDZ has been featured in much research work, research on its long-term evolution, especially healing and sealing that may occur due to creep (i.e., time-dependent deformation), is relatively rare. Numerical studies considering geological disposal in rock salt found that damage in the EDZ could heal and seal due to creep (Blanco-Martín, et al., 2015a; Blanco-Martín et al., 2015b; Blanco-Martín et al., 2018; Tounsi et al., 2023). Also, laboratory experiments showed that creep decreased the permeability of shale (Zhang et al., 2021).

Shale is attractive as host rock for the geological disposal of nuclear waste considering its low permeability. Creep of shales has been found to follow the so-called power-law (Sone & Zoback, 2011; Li & Ghassemi, 2012; Nopola & Roberts, 2016; Rybacki et al., 2017; Benge et al., 2021), in which rates of creep strain increments increase and decrease with the deviatoric stress and time (or cumulative creep strains), respectively, raised to the power of some constants. To model power-law creep, the Norton-Bailey model (Bailey, 1935; Norton, 1929), which is equivalently referred to as the Lemaitre-Menzel-Schreiner model (Lemaitre, 1979; Menzel & Schreiner, 1977), can be used; this creep model is considered suitable if expected deviatoric stress levels are below a certain level (e.g., <60 MPa), and such a deviatoric stress level is not expected to be reached in geological nuclear waste repositories during the post-closure period (e.g., Rutqvist, 2020).

Our previous work using the Norton-Bailey model showed that shale creep could significantly decrease stress levels in a geological nuclear waste repository in the long term, leading to decreased permeability in the EDZ, and it could also enhance the compaction of bentonite in the EBS (Sasaki & Rutqvist, 2022). This numerical work was, however, carried out with the assumption that shale creep is isotropic, i.e., it ignores the presence of bedding in shale. The Norton-Bailey model also implicitly assumes no creep-induced volumetric deformation (i.e., no compaction or expansion due to creep), which is against some experimental data (Chang & Zoback, 2009; Li & Ghassemi, 2012; Sone & Zoback, 2013b, 2014). These commonly applied but somewhat unrealistic assumptions might have had a significant impact on the simulation results. Note that an anisotropic creep model could produce no volumetric deformation, as anisotropic creep simply means creep magnitude varying with the loading direction with respect to the bedding; an additional term is required to incorporate volumetric deformation.

In order to understand the effects of these assumptions, an anisotropic power-law creep model is needed. Choo et al. (2021) developed a bi-layer model for simulating anisotropic creep in which so-called Duvaut-Lions approach (Duvaut & Lions, 1976) was implemented with the Cam-Clay plastic potential function (Roscoe & Burland, 1968; Schofield & Wroth, 1968), which is suited for simulating volumetric compaction of soils and rocks, while Borja et al. (2020) developed a heterogenous two-material model in which either the Duvaut-Lions or Perzyna approach (Perzyna, 1966) was implemented with the Cam-Clay potential function. Their models are not, however, equipped with capabilities to generate creep strain increments that obey the power-law creep. Another model developed by Barla et al. (2012) obeys the power-law creep but lacks anisotropic characteristics. A simpler approach to modeling anisotropy was proposed by Mánica et al. (2016,

Table 5
The parameters modified for the long-term creep case.

	Haynesville-1 V	Barnett-1H
m (-)	0.60	0.60
A (s^{-1})	4.9E-15	1.1E-15

Table 6
The parameters modified for the isotropic creep case.

	Haynesville-1 V	Barnett-1H
c_H (-)	1	1
M (-)	0	0

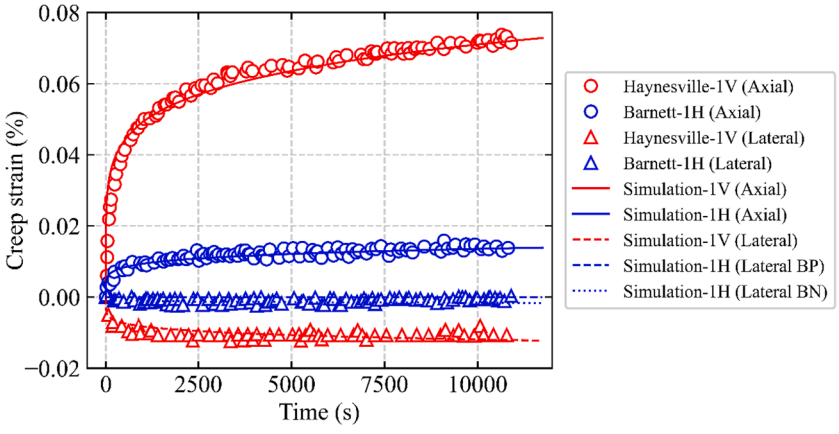

Fig. 3. Results of the model calibration for two shales: Haynesville-1 V and Barnett-1H shales.

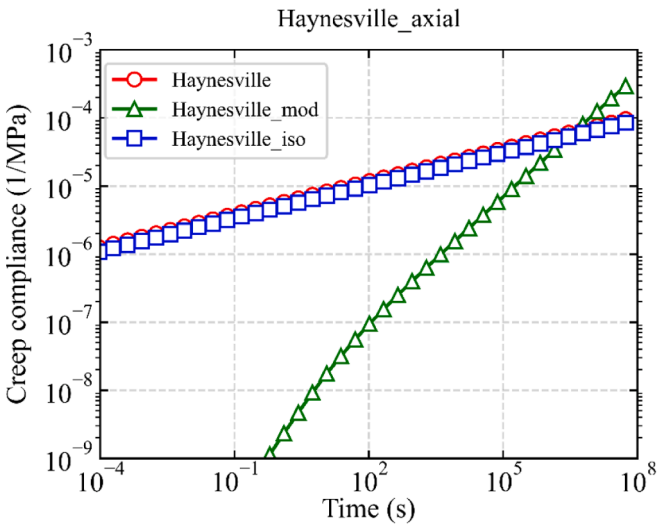

(a)

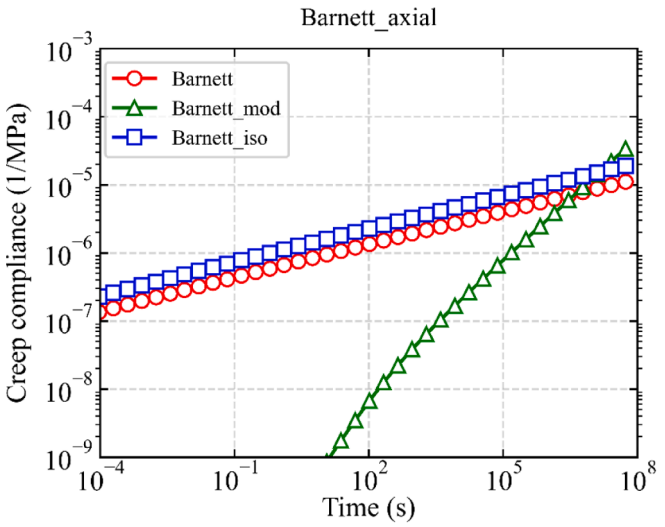

(b)

Fig. 4. Calculated axial creep compliance of the (a) Haynesville-1 V and (b) Barnett-1H shales in the simulation of the triaxial testing ("mod" and "iso" in the figure legends indicate the long-term and isotropic creep cases, respectively).

2017), who modified components of the Cauchy stress tensor with coefficients to defined the anisotropic stress tensor. This approach is equipped with a strain-hardening power-law creep formulation (and capacity to incorporate creep-induced volumetric deformation), and it was implemented by them and also by Jung et al. (2022) to simulate the mechanical behavior of a drift excavated in a claystone formation.

The present research extends our previous work with an anisotropic shale creep model based on the concepts of Mánica et al. (2016, 2017) incorporated with the Cam-Clay potential function for creep-induced volumetric deformation. The objective is to understand the effects of anisotropic shale creep on the long-term, THM coupled behavior of a geological nuclear waste repository, especially on the evolution of stress and permeability in the formation near waste emplacement drifts. The outcome of this research will benefit the performance assessment (PA) of

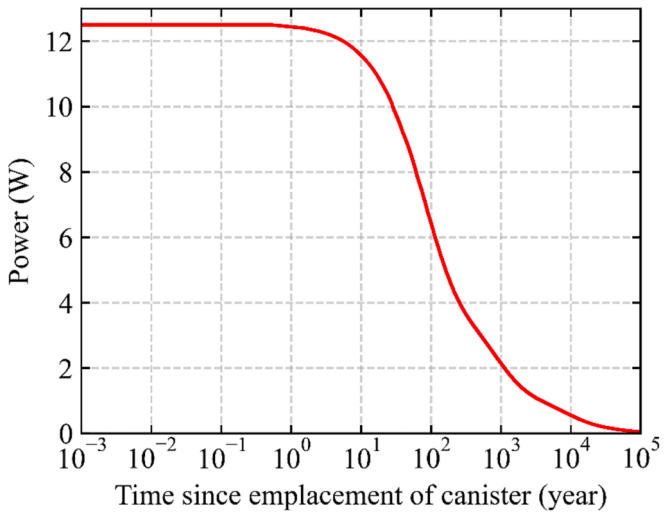

Fig. 5. The time-varying heat source assigned to each of the sixteen canister elements, representing the decay heating of nuclear waste packages.

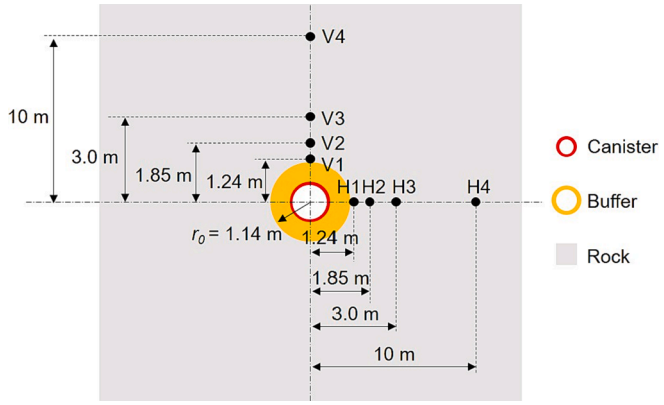

Fig. 6. The vertical (V1-4) and horizontal (H1-4) locations in the formation where results were extracted.

geological nuclear waste repositories by increasing its reliability and robustness. Numerical simulations were carried out with a THM coupled simulator, TOUGH-FLAC (Rinaldi et al., 2022; Rutqvist, 2011), with the new anisotropic shale creep model calibrated against experimental data. Using the results of the anisotropic creep simulations as the base case, comparisons were performed between the base case and the no creep (i.e., elastic), isotropic creep, and long-term anisotropic creep simulation cases, in order to gain insights into the effects of anisotropic shale creep on the PA of a geological nuclear waste repository in shale. Note that 'long term' in this study is arbitrarily defined as time after 1,000 years after canister emplacement in a geological repository, where temperatures and pore pressure are expected to start coming down to the initial in-situ levels. Details of the numerical model, the governing equations of the TOUGH-FLAC simulator, and the anisotropic shale creep model are provided in the following section.

2. Numerical modeling

2.1. Model geometry

Fig. 1 shows an overview of the numerical model of a generic nuclear waste repository with horizontal drifts for nuclear waste emplacement. Although it is actually a three-dimensional (3D) model, the third dimension (in the out-of-plane direction) is constrained, namely, there is no displacement, fluid flow, or thermal flux in this direction; hence, the

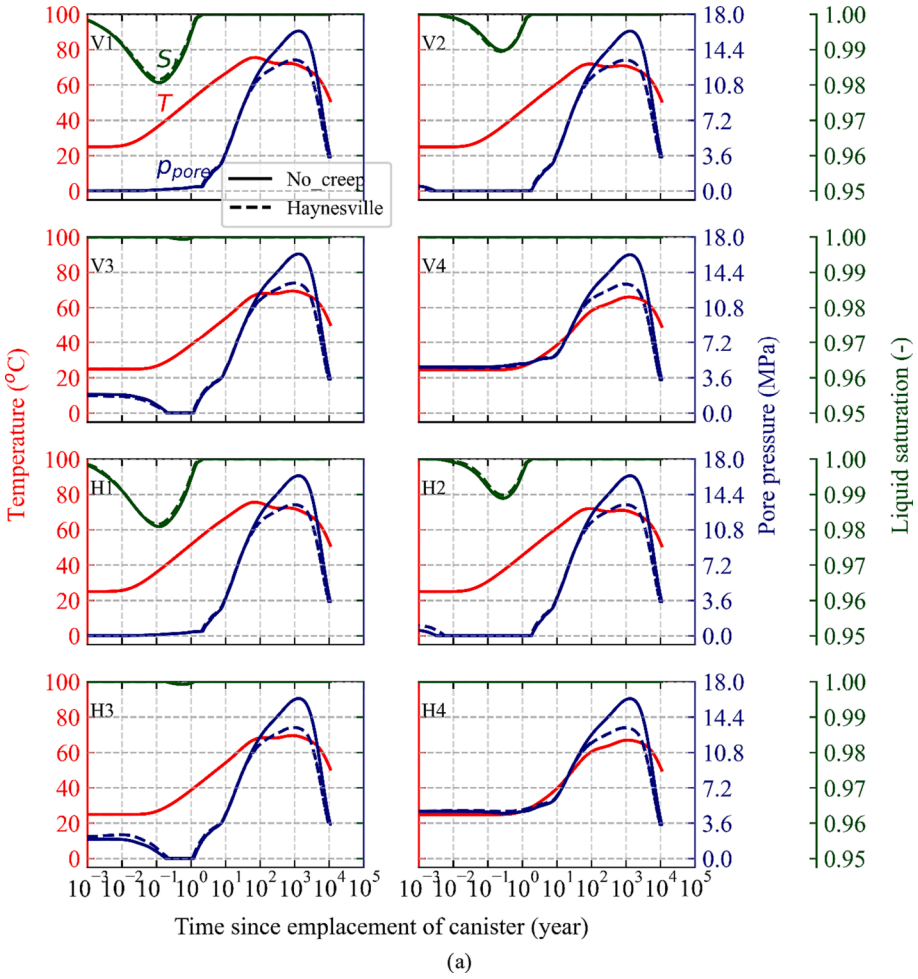

Fig. 7. The evolution of temperature, pore pressure, and liquid-phase saturation at selected locations in the formation with (a) the Haynesville and (b) the Barnett shale properties (anisotropic creep vs. no creep cases).

model is effectively a 2D plane-strain model. The model consists of canister, bentonite buffer, and rock (i.e., a shale formation) components. The canister was assumed to be disposed of in a subsurface drift that is located at a depth of 500 m from the ground surface, and the space in the drift between the canister and rock was assumed to be filled with the bentonite buffer to form the engineered barrier system (EBS). The diameters of the concentric canister and drift are 0.9 m and 2.28 m, respectively. The total depth and lateral length of the model are 1,000 m and 50 m, respectively. Because the entire repository was assumed to consist of multiple drifts drilled parallel to one another at the same depth with fixed lateral spacing, this model represents a single 'slice' of the entire repository with a drift-to-drift spacing of 50 m. To make this model representative of the entire repository, relevant boundary conditions were applied, namely, the displacements, fluid flow, and thermal flux normal to the lateral boundary surfaces were assumed to be nonexistent. Other boundary conditions included a pore pressure and a temperature of 0.1 MPa and 10 °C at the ground surface and of 9.91 MPa and 40 °C at the bottom of the model, respectively, and constant gradients of pore pressure and temperature along the depth. Mechanically, the displacements normal to the bottom boundary were fixed, while on the top boundary (i.e., the ground surface) a constant surface pressure of 0.1 MPa was applied. Last but not least, the rock/bentonite and bentonite/canister interfaces were assumed to be bonded at all times, i.e., the displacements remain continuous across these interfaces.

2.2. Thermo-hydromechanically coupled simulator

A THM coupled simulator, TOUGH-FLAC (Rutqvist, 2011; Rinaldi et al., 2022), was used to create the repository model shown in Fig. 1. It is a sequentially-coupled simulator where the thermo-hydrological (TH) calculations are performed in the TOUGH3 code, whereas the mechanical (M) calculations in the FLAC3D software. TOUGH3 controls the coupling sequence, as in each time step, it first completes a TH calculation and passes the converged values of TH variables, such as pore pressure and temperature, to FLAC3D. FLAC3D then performs a mechanical (M) calculation to obtain the converged values of M variables, such as stress and strain increments, using the fixed values of TH variables received from TOUGH3. Finally, some TH parameters that are dependent on the values of M variables, such as permeability and porosity, are updated before TOUGH3 performs TH calculation for the next time step, and the simulation continues in this sequentially coupled way. More details of the sequential coupling approach adopted in TOUGH-FLAC are provided in the literature (Kim et al., 2011, 2012a, 2012b; Rinaldi et al., 2022).

A summary of the governing equations solved by the TOUGH3 and FLAC3D are provided in the following subsections. A brief explanation of the THM coupling among the governing equations is also provided, followed by the introduction of the anisotropic creep constitutive model, and finally by the modelling steps for simulating the construction and post-closure periods of the repository.

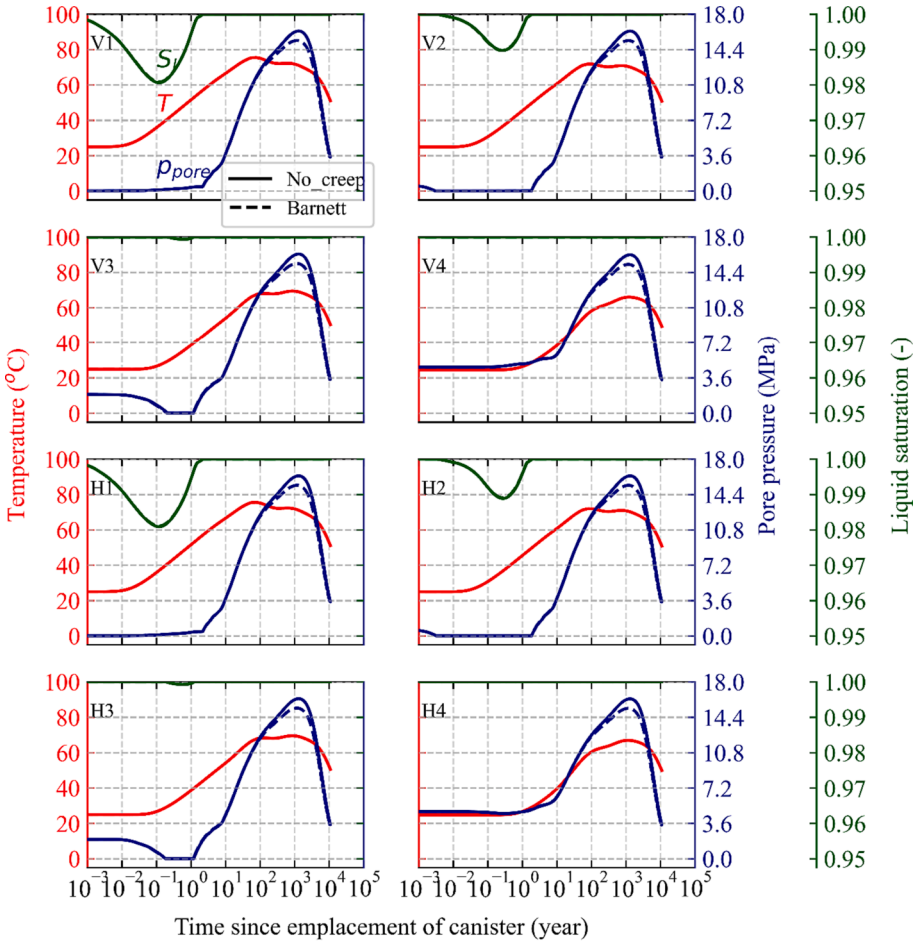

(b)

Fig. 7. (*continued*).

2.2.1. *Thermo-hydrological governing equations*

The mass- and energy-balance equations handled by TOUGH3 are of the same form as shown below:

$$\frac{d}{dt}\int_V M^\kappa dV = \int_\Gamma \boldsymbol{f}^\kappa \bullet \boldsymbol{n} d\Gamma + \int_V q^\kappa dV \tag{1}$$

where V (m^3) is a closed finite control volume of the system under study, Γ (m^2) is the boundary surface of the closed volume, $\boldsymbol{n}$ (-) is the surface normal vector of an infinitesimal area ($d\Gamma$) of the boundary surface, M^κ (kg/m^3 or J/m^3) is the mass of component $\kappa(\kappa = 1, 2, \cdots)$ (e.g., water, air, etc.) or energy ($\kappa = h$), $\boldsymbol{f}^\kappa$ (kg/s/m^2 or W/m^2) is a vector denoting mass flux ($\kappa = 1, 2, \cdots$) or heat flux ($\kappa = h$), and q^κ (kg/s/m^3 or W/m^3) is a sink/source of mass or energy.

The accumulation (M^κ) and flux ($\boldsymbol{f}^\kappa$) terms of the mass balance are expressed as follows:

$$M^\kappa = \phi \sum_\beta S_\beta \rho_\beta X_\beta^\kappa + (1-\phi)\rho_S \rho_l X_l^\kappa K_d \tag{2}$$

where ϕ (-) is porosity, S_β (-) is the degree of saturation of phase β (=gas or liquid), ρ_β (kg/m^3) is the density of phase β, X_β^κ (-) is the mass fraction of component κ in phase β, ρ_S (kg/m^3) is the solid-phase grain density, ρ_l (kg/m^3) is the density of liquid phase, X_l^κ (-) is the mass fraction of component κ in liquid phase, K_d (m^3/kg) is the liquid phase distribution coefficient, and

$$\boldsymbol{f}^\kappa = \sum_\beta X_\beta^\kappa \boldsymbol{f}_\beta \tag{3}$$

where $\boldsymbol{f}_\beta$ (kg/s/m^2) is the mass flux of phase β, which is given by a multiphase version of Darcy's law expressed in the following form:

$$\boldsymbol{f}_\beta = -k\frac{k_{r\beta}\rho_\beta}{\mu_\beta}\left(\nabla P_\beta - \rho_\beta \boldsymbol{g}\right) \tag{4}$$

where k (m^2) is the absolute permeability, $k_{r\beta}$ (-) is the relative permeability of phase β, μ_β (Pa·s) is the dynamic viscosity of phase β, P_β (Pa) is the fluid pressure of phase β, which is calculated as the sum of a reference pressure, P (Pa) (i.e., usually, gas pressure), and capillary pressure, P_{cap} (Pa) (i.e., $P_\beta = P + P_{cap}$), and $\boldsymbol{g}$ (m/s^2) is a vector denoting gravitational acceleration.

The following relative permeability and capillary pressure functions were used in this study.

$$k_{rl} = \begin{cases} \sqrt{S^*}\left(1-\left(1-(S^*)^{1/\lambda_k}\right)^{\lambda_k}\right)^2 & \text{if } S_l < S_{ls} \\ 1 & \text{if } S_l \geq S_{ls} \end{cases}$$
$$k_{rg} = \begin{cases} 1 - k_{rl} & \text{if } S_{gr} = 0 \\ (1-\widehat{S})^2\left(1-\widehat{S}^2\right) & \text{if } S_{gr} > 0 \end{cases} \tag{5}$$

where

$$S^* = (S_l - S_{lr})/(S_{ls} - S_{lr}) \tag{6}$$

$$\widehat{S} = (S_l - S_{lr})/(1 - S_{lr} - S_{gr}) \tag{7}$$

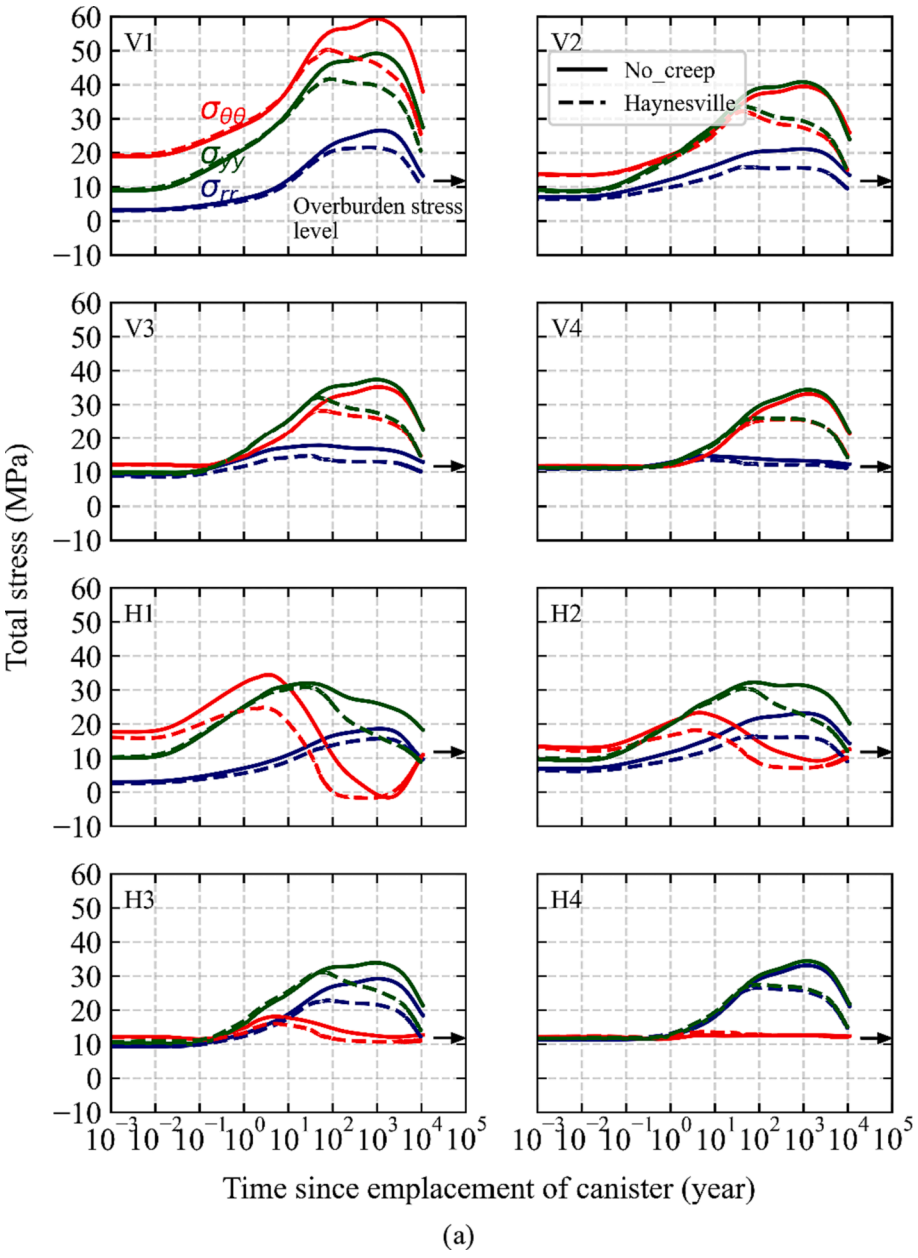

Fig. 8. The evolution of stresses at selected locations in the formation with the Haynesville shale properties (anisotropic creep vs. no creep cases): (a) total stress; (b) mean effective and deviatoric stresses.

where k_{rl} (-) and k_{rg} (-) are the relative permeability of the liquid and gas phases, respectively, λ_k (-) is a van Genuchten parameter (which is expressed as m in the original notation in van Genuchten (1980)), S_l (-) is the liquid-phase saturation, S_{lr} (-) is the residual (i.e., minimum) liquid-phase saturation, S_{ls} (-) is the saturated (i.e., maximum) liquid-phase saturation, S_{gr} (-) is the residual gas-phase saturation, and

$$P_{cap} = -P_0\left(\left(S^*\right)^{-1/\lambda_k} - 1\right)^{1-\lambda_k} \tag{8}$$

where P_0 (Pa) is a parameter related to the air entry pressure. Note that the maximum capillary pressure value, P_{max} (Pa), was specified such that $-P_{max} \le P_{cap} \le 0$.

Mass transport is driven not only by Darcy flow but also by diffusion, f^{κ}_{diff} (kg/s/m^2), which is expressed as follows:

$$f^{\kappa}_{diff} = -\phi\sum_{\beta}\tau_0\tau_\beta\rho_\beta d^{\kappa}_{\beta}\nabla X^{\kappa}_{\beta} \tag{9}$$

where $\tau_0\tau_\beta$ (-) is a tortuosity factor, which is the product of a porous medium factor (τ_β) and a phase-saturation factor (τ_β), d^{κ}_{β} (m^2/s) is the molecular diffusion coefficient of component κ in phase β, $\nabla X^{\kappa}_{\beta}$ (m^{-1})is the gradient of the mass fraction of component κ in phase β. Note that in this study, $\tau_0\tau_\beta = S_\beta$ was assumed.

Finally, vapor pressure lowering due to capillary pressure and phase adsorption was considered via the following equation:

$$P_v = P_{sat}\exp\left(\frac{M_w P_{cap}}{\rho_l R(T + 273.15)}\right) \tag{10}$$

where P_v (Pa) is vapor pressure, P_{sat} (Pa) is the saturation vapor pressure, M_w (kg/mol) is the molecular weight of water, R (J/mol/^{o}C) is the

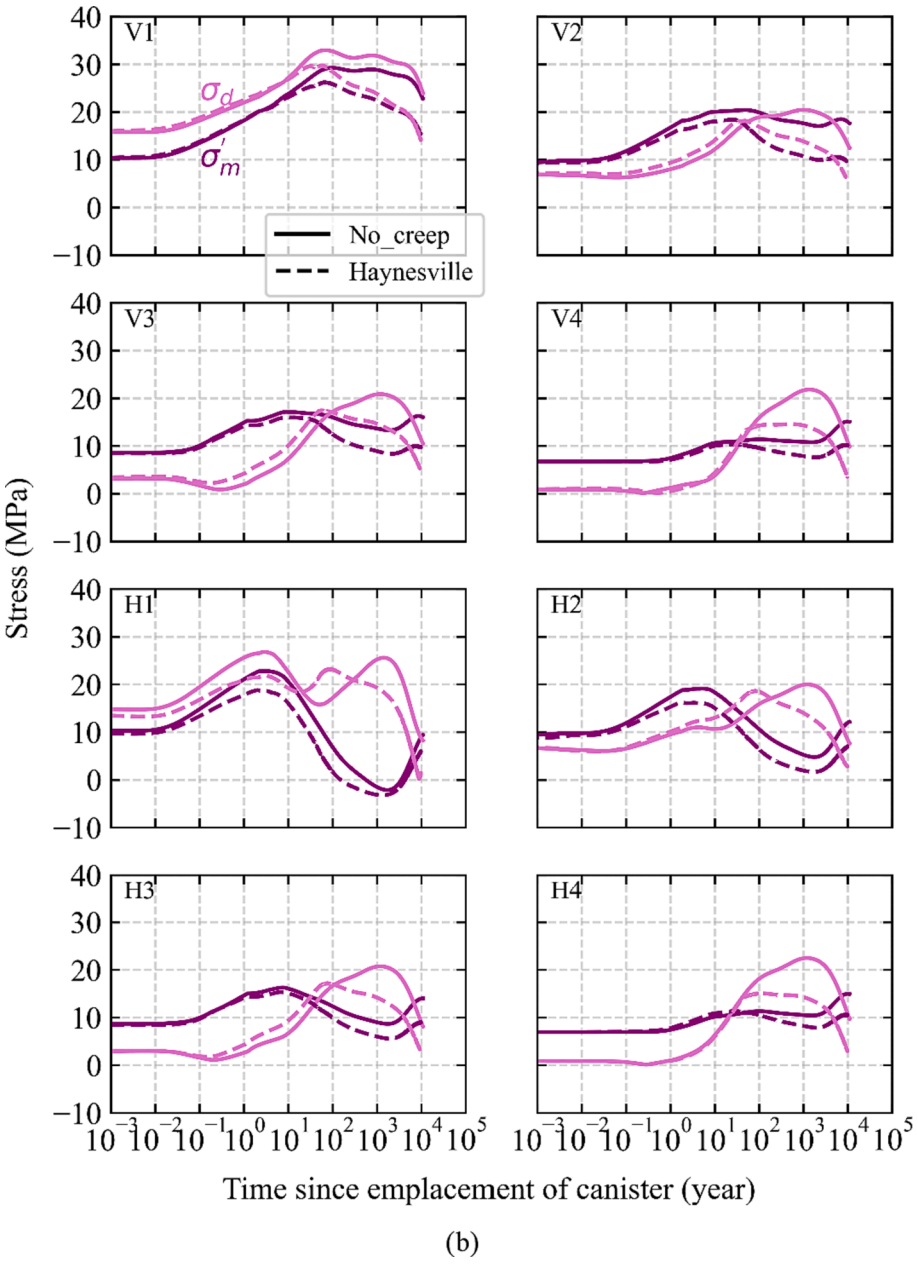

Fig. 8. (*continued*).

universal gas constant, and T (°C) is temperature.

The accumulation (M^h) and flux (f^h) terms of the energy balance are expressed as follows:

$$M^h = (1-\phi)\rho_S C_S T + \phi \sum_\beta S_\beta \rho_\beta U_\beta \tag{11}$$

where C_S (J/kg/°C) is the specific heat of solid grains, U_β (J/kg) is the specific internal energy of phase β, and

$$f^h = -\lambda \nabla T + \sum_\beta h_\beta f_\beta + f_\sigma \sigma_0 \nabla T^4 \tag{12}$$

where λ (W/(m·°C)) is the effective thermal conductivity, h_β (J/kg) is the specific enthalpy in phase β, f_σ (-) is the radiant emittance factor, and σ_0 (W/m^2/K^4) is the Stefan-Boltzmann constant. Note that, in this study, radiation heat transfer was ignored by setting $f_\sigma = 0$.

Table 1 lists the thermo-hydrological parameters and their values assumed in this study. Note that anisotropic permeability and thermal conductivity (i.e., parallel (//) and normal (⊥) to bedding) were considered only in the rock component.

2.2.2. Mechanical governing equations

The mechanical governing equation solved by FLAC3D is the equation of motion as shown below:

$$\nabla \bullet \boldsymbol{\sigma} + \rho_b \boldsymbol{g} = \rho_b \frac{d\boldsymbol{v}_R}{dt} \tag{13}$$

where $\boldsymbol{\sigma}$ (Pa) is the Cauchy stress tensor, ρ_b (kg/m^3) is the bulk density ($= \phi \sum_\beta \rho_\beta S_\beta + (1-\phi)\rho_R$), and $\boldsymbol{v}_R$ (m/s) is the velocity vector of the solid phase.

Stress is usually updated in an incremental way so as to incorporate any nonlinearity during mechanical deformation. Stress increments are related to strain increments via a mechanical constitutive model, a general form of which can be represented as follows:

$$d\boldsymbol{\sigma} = \mathbb{C} \bullet\bullet \, d\boldsymbol{\epsilon}^e \tag{14}$$

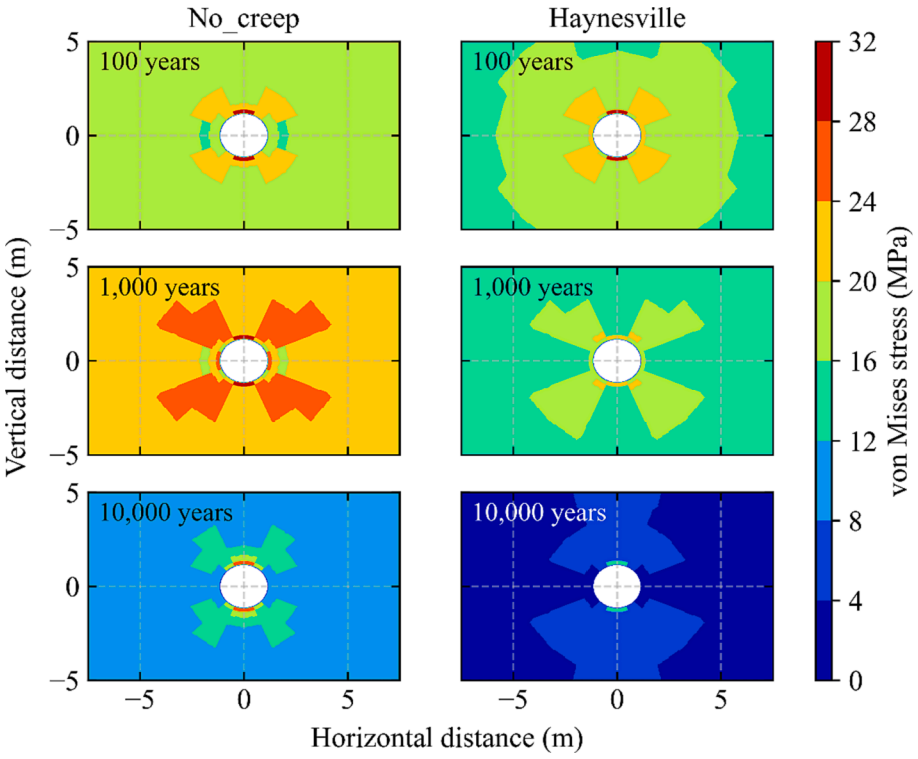

Fig. 9. Distributions of the deviatoric stress in the formation with the Haynesville shale properties (no creep cases vs. anisotropic creep cases) at different times (100 vs. 1,000 vs. 10,000 years).

where $d\boldsymbol{\sigma}$ (Pa) is the second-order tensor of stress increments, $\mathbb{C}$ (Pa) is the fourth-order tensor of elastic moduli, and $d\epsilon^e$ (-) is the second-order tensor of elastic strain increments, which are defined as total strains minus thermal strains (i.e., $d\epsilon^e = d\epsilon^T - d\epsilon^{th}$). The canister (steel) and bentonite were assumed to follow the isotropic linear elasticity, which has only two independent elastic parameters: Young's modulus and Poisson's ratio. Their values are provided in Table 2. Note that any plasticity in either the canister steel or bentonite buffer was not considered in this study.

For the bentonite, swelling was assumed to occur due to changes in the liquid-phase saturation as described in the following equation:

$$d\epsilon^s = \beta_s \Delta S_l \boldsymbol{E} \tag{15}$$

where $d\epsilon^s$ (-) is the second-order tensor of swelling strain increments, β_s (-) is a swelling coefficient, ΔS_l (-) is an increment in the liquid-phase saturation, and $\boldsymbol{E}$ (Pa) is the unit tensor of order two. Stress updates are performed as shown in Eq. (14) with elastic strain increments calculated by $d\epsilon^e = d\epsilon^T - d\epsilon^s - d\epsilon^{th}$.

For the rock, cross-anisotropic (i.e., transverse isotropic) elasticity and creep are considered. Their details are presented in one of the following subsections.

2.2.3. Thermo-hydro-mechanical coupling

Herein some of the equations that couple the governing equations are presented. First, the coupling from the thermal to mechanical process is performed via thermal strain as shown earlier (e.g., $d\epsilon^e = d\epsilon^T - d\epsilon^{th}$), while the coupling from hydrological to mechanical process via the effective stress shown below:

$$\boldsymbol{\sigma}' = \boldsymbol{\sigma} - \alpha_{BW} P \boldsymbol{E} \tag{16}$$

where $\boldsymbol{\sigma}'$ (Pa) is the effective stress tensor of order two, $\boldsymbol{\sigma}$ (Pa) is the total stress tensor of order two, α_{BW} (-) is the Biot-Willis coefficient, P (Pa) is pore pressure, which is defined in this study as $P = \max\left(p_l, p_g\right)$ where p_l and p_g are the liquid- and gas-phase pressure, respectively. Note also that $\alpha_{BW} = 1$ was assumed for all the model components including the shale formation. Also note that this study assumes an isotropic Biot-Willis coefficient; in reality, it is anisotropic for transversely isotropic (i.e., cross-anisotropic) material like shale, having two independent components. The difference between the values of the two components are, however, usually small as shown in Cheng (1997). Hence, the assumption of an isotropic Biot-Willis coefficient should be valid. Since the effective stress governs the mechanical behavior of porous material, it is used, instead of the total stress, in the mechanical constitutive equations for the rock and bentonite.

Another essential coupling from the mechanical to thermo-hydrological process is performed via porosity changes as shown in the equation below:

$$d\phi = \left(\frac{\alpha_{BW}^2 + (\alpha_{BW} - \phi)(1 - \alpha_{BW})}{K}\right) dP + 3\alpha_S \phi dT - \Delta\phi_c \tag{17}$$

where $d\phi$ (-) is an increment in porosity, K (Pa) is the bulk modulus of porous material, α_S (1/°C) is the linear thermal expansion coefficient of solid grains, and $\Delta\phi_c$ (-) is the porosity correction specifically needed for the implementation of the sequential coupling between TOUGH3 and FLAC3D (Kim et al., 2011; 2012a, 2012b; Xu et al., 2020; Rinaldi et al., 2022), which is expressed as follows:

$$\Delta\phi_c = -\frac{\alpha_{BW}}{K}\left(K d\epsilon_V - \alpha_{BW} dP - 3\alpha K dT\right) \tag{18}$$

where $d\epsilon_V$ (-) is an increment in the volumetric strain $\left(= \mathrm{tr}\left(d\epsilon^T\right)\right.$ where $d\epsilon^T$ (-) is the total strain increment tensor), and α (1/°C) is the linear thermal expansion coefficient of porous material, which was assumed to be equal to that of the solid grains in this study (i.e., $\alpha = \alpha_S$).

Finally, permeability was assumed to be a function of mechanical stresses as follows (Rutqvist et al., 2009):

$$k = \left(k_r + \Delta k_{max} \exp\left(\beta_1 \sigma_m'\right)\right) \exp\left(\gamma \langle \sigma_d - \sigma_{d,crit} \rangle\right) \tag{19}$$

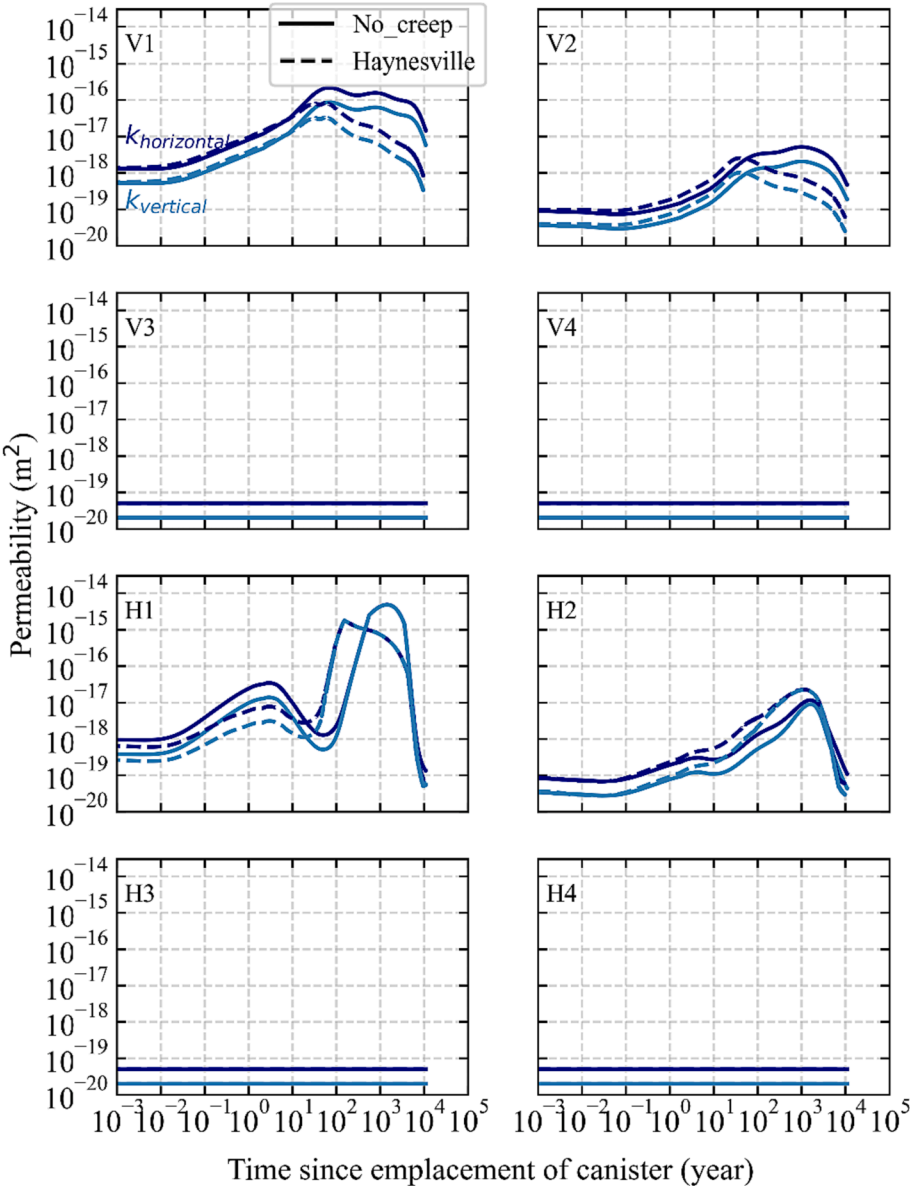

Fig. 10. The evolution of permeability at selected locations in the formation with the Haynesville shale properties (anisotropic creep vs. no creep cases).

where k_r (m^2) is the residual permeability, Δk_{max} (m^2) is the maximum permeability increment (which is achieved at zero mean effective stress), β_1 (Pa^{-1}) is a mean effective stress factor, $\sigma_m^{'}$ (Pa) is the mean effective stress ($=\mathrm{tr}(\boldsymbol{\sigma}^{'})/3$), γ (Pa^{-1}) is a deviatoric stress factor, σ_d (Pa) is the deviatoric stress ($=\sqrt{(3/2)\boldsymbol{S}:\boldsymbol{S}}$ where $\boldsymbol{S}=\boldsymbol{\sigma}-\mathrm{tr}(\boldsymbol{\sigma})\boldsymbol{E}/3$), and $\sigma_{d,crit}$ (Pa) is a critical deviatoric stress. The $\langle\rangle$ operator denotes the Macaulay bracket, where $\langle f\rangle = f$ if $f>0$ and $\langle f\rangle = 0$ in all other cases. The values of the permeability parameters are listed in Table 3. Note that this permeability function was applied only to the excavation damaged zone (EDZ) in the formation around the drift. The area of EDZ was assumed to be bounded by a cylinder coaxial to the drift with its radius being twice that of the drift. Although this assumption is based on the findings of Bossart et al. (2002), the shape of the EDZ could be non-circular, which could have some impacts on the simulation results. Permeability was assumed to remain constant in the canister, bentonite, or the formation outside of the EDZ.

2.3. Anisotropic creep constitutive model

This section introduces an anisotropic creep constitutive model for shale. The model assumes that shale is cross-anisotropic (i.e., transversely isotropic) owing to its bedding as shown in Fig. 2. The figure also shows two sets of coordinates: the local and global coordinates. The local coordinates are aligned with the shale bedding, while the global coordinates with the direction of gravity.

The formulation of the anisotropic creep model begins with defining the stress tensor for an infinitesimally small element. As the mechanical behavior of porous material, including shale, is governed by the effective stress (rather than the total stress), the effective stress tensor is defined herein. Shown below using a matrix notation are the components of the effective stress tensor defined in the global Cartesian coordinates (x, y, z).

$$\left(\sigma_{G,ij}^{'}\right)=\begin{pmatrix}\sigma_{xx}^{'} & \sigma_{xy}^{'} & \sigma_{xz}^{'}\\ \sigma_{xy}^{'} & \sigma_{yy}^{'} & \sigma_{yz}^{'}\\ \sigma_{xz}^{'} & \sigma_{yz}^{'} & \sigma_{zz}^{'}\end{pmatrix} \tag{20}$$

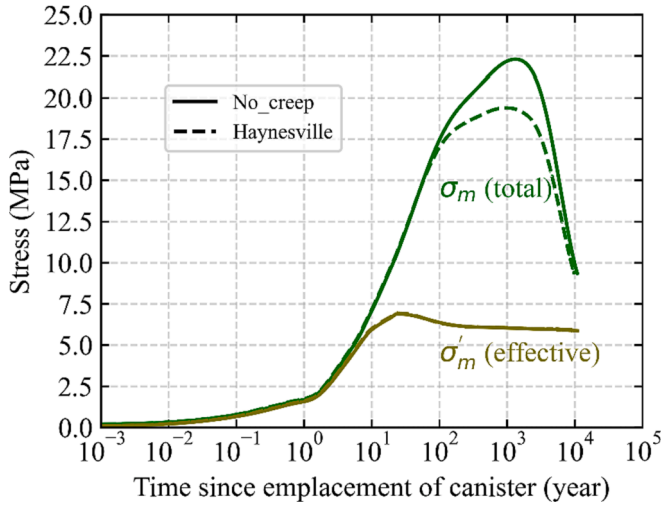

Fig. 11. The evolution of stresses in the bentonite buffer in the formation with the Haynesville shale properties (anisotropic creep vs. no creep cases). Note that the solid and dashed lines for the effective stress are on top of each other.

where $\left(\sigma'_{G,ij}\right)$ represents the components of the effective stress tensor, $\boldsymbol{\sigma}'$(Pa), in the global Cartesian coordinates.

As the global coordinates are not aligned with the bedding, they need to be rotated (Fig. 2) to obtain the components in the local Cartesian coordinates (*1*, *2*, *3*). Note that the *y*-axis of the global coordinates is assumed to align with the *2*-axis of the local coordinates.

$$\left(\sigma'_{L,ij}\right) = \begin{pmatrix} \sigma'_{11} & \sigma'_{12} & \sigma'_{13} \\ \sigma'_{12} & \sigma'_{22} & \sigma'_{23} \\ \sigma'_{13} & \sigma'_{23} & \sigma'_{33} \end{pmatrix} \tag{21}$$

where $\left(\sigma'_{L,ij}\right)$ represents the components of the effective stress tensor,$\boldsymbol{\sigma}'$ (Pa), in the local Cartesian coordinates. Coordinate transformation (i.e., rotation) is carried out as shown in the following equation:

$$\boldsymbol{\sigma}'_L = \boldsymbol{Q} \bullet \boldsymbol{\sigma}'_G \bullet \boldsymbol{Q}^T \tag{22}$$

where $\boldsymbol{\sigma}'_L$ (Pa) and $\boldsymbol{\sigma}'_G$ (Pa) are the effective stress tensor in the local and global coordinates, respectively, and $\boldsymbol{Q}$ (-) is a coordinate transformation tensor and its components are expressed as follows for the rotation shown in Fig. 2.

$$(Q_{ij}) = \begin{pmatrix} \cos\beta & 0 & \sin\beta \\ 0 & 1 & 0 \\ -\sin\beta & 0 & \cos\beta \end{pmatrix} \tag{23}$$

where β (°) is a rotation angle.

To define the cross-anisotropic stress tensor (Mánica et al., 2016), the components of the local effective stress tensor are scaled with coefficients (c_V, c_H, c_S) as shown below. Note that the coordinates for the anisotropic tensor remains the local Cartesian coordinates (*1*, *2*, *3*).

$$\left(\sigma'_{A,ij}\right) = \begin{pmatrix} c_H\sigma'_{11} & \sigma'_{12} & c_S\sigma'_{13} \\ \sigma'_{12} & c_H\sigma'_{22} & c_S\sigma'_{23} \\ c_S\sigma'_{13} & c_S\sigma'_{23} & c_V\sigma'_{33} \end{pmatrix} \tag{24}$$

where $\left(\sigma'_{A,ij}\right)$ represents the components of the cross-anisotropic effective stress tensor,$\boldsymbol{\sigma}'_A$ (Pa).

Next, an anisotropic viscoplastic (i.e., creep) potential function is defined using the modified Cam-Clay plastic potential function (Roscoe & Burland, 1968; Schofield & Wroth, 1968) as shown below:

$$f^2 = q_A^2 + M^2 p'_A\left(p'_A + p_0\right) \tag{25}$$

where M (-) is the critical state frictional constant, which is a function of the internal friction angle of porous material, p_0 (Pa) is the so-called preconsolidation pressure, which is related to the maximum compressive stress experienced by porous material, and q_A (Pa) and p'_A (Pa) are the anisotropic deviatoric and mean effective stresses defined as follows:

$$q_A = \sqrt{\frac{3}{2}\boldsymbol{S}_A : \boldsymbol{S}_A} \tag{26}$$

$$p'_A = \frac{1}{3}\mathrm{tr}\left(\boldsymbol{\sigma}'_A\right) \tag{27}$$

where $\boldsymbol{S}_A$ (Pa) is the anisotropic deviatoric stress tensor shown below:

$$\boldsymbol{S}_A = \boldsymbol{\sigma}'_A - p'_A\boldsymbol{E} \tag{28}$$

where $\boldsymbol{E}$ (-) is the unit tensor of order two. Note that the ':' operator in Eq. (26) represents the scalar product of two second-order tensors (e.g., $\boldsymbol{a}\otimes\boldsymbol{b} : \boldsymbol{c}\otimes\boldsymbol{d} = (\boldsymbol{a}\bullet\boldsymbol{c})(\boldsymbol{b}\bullet\boldsymbol{d})$ where $\boldsymbol{a},\boldsymbol{b},\boldsymbol{c},\boldsymbol{d}$ are arbitrary vectors).

We selected the Cam-Clay model since it can capture the volumetric deformation of soil/rock. In shale, the Cam-Clay model should be particularly suitable, as the compaction supposedly occurs mainly in the soft clay layers. Using the above-defined anisotropic Cam-Clay potential function, anisotropic creep strain increments are calculated following the Perzyna approach (Perzyna, 1966), which can be expressed in the following form (Chang & Zoback, 2010):

$$\boldsymbol{d}\dot{\epsilon}^{vp}_L = \langle\varphi(f)\rangle\frac{\partial f}{\partial\boldsymbol{\sigma}'_L} \tag{29}$$

where $\boldsymbol{d}\dot{\epsilon}^{vp}_L$ (-) is the viscoplastic (i.e., creep) strain increment tensor of order two (defined in the local coordinates), and $\varphi(f)$ is an arbitrary function of f. The $\langle\rangle$ operator is the Macaulay bracket, where $\langle\varphi(f)\rangle = \varphi(f)$ if $\varphi(f) > 0$ and $\langle\varphi(f)\rangle = 0$ in all other cases. The function, $\varphi(f)$, was determined such that the creep strain increments follow those of the power-law creep, which has been found suitable for modelling shale creep (Sone & Zoback, 2011; Li & Ghassemi, 2012; Nopola & Roberts, 2016; Rybacki et al., 2017; Benge et al., 2021). Consequently, the creep strain increment tensor for cross-anisotropic shale was determined as follows:

$$\boldsymbol{d}\dot{\epsilon}^{vp}_L = mA^{\frac{1}{m}}\left(\frac{\epsilon_{cr}+\epsilon_{shift}}{t_{ref}}\right)^{\frac{m-1}{m}}\left\langle\frac{f}{\sigma_{ref}}\right\rangle^{\left(\frac{n}{m}\right)}\frac{\partial f}{\partial\boldsymbol{\sigma}'_L} \tag{30}$$

where m (-) and n (-) are power-law exponents, A (s^{-1}) is a power-law coefficient, ϵ_{cr} (-) is the cumulative creep strain, ϵ_{shift} (-) is a creep strain shift that is introduced to avoid division by zero when $\epsilon_{cr} = 0$ at $t = 0$, $t_{ref}(=1)$ (s) and $\sigma_{ref}(=1)$ (Pa) are coefficients that are required merely to make the units of both sides of Eq. (30) consistent with each other. Note that the above anisotropic formulation reverts to the isotropic power-law creep formula (Sasaki & Rutqvist, 2022), which is often referred to as the Norton-Bailey model or the Lemaitre-Menzel-Schreiner model when $c_V = c_H = c_S = 1$ and $M = 0$ are specified. Moreover, note that the shear components of strains calculated by Eq. (29) and (30) are engineering shear strains; they need to be multiplied with 0.5 to convert them into scientific shear strains as follows.

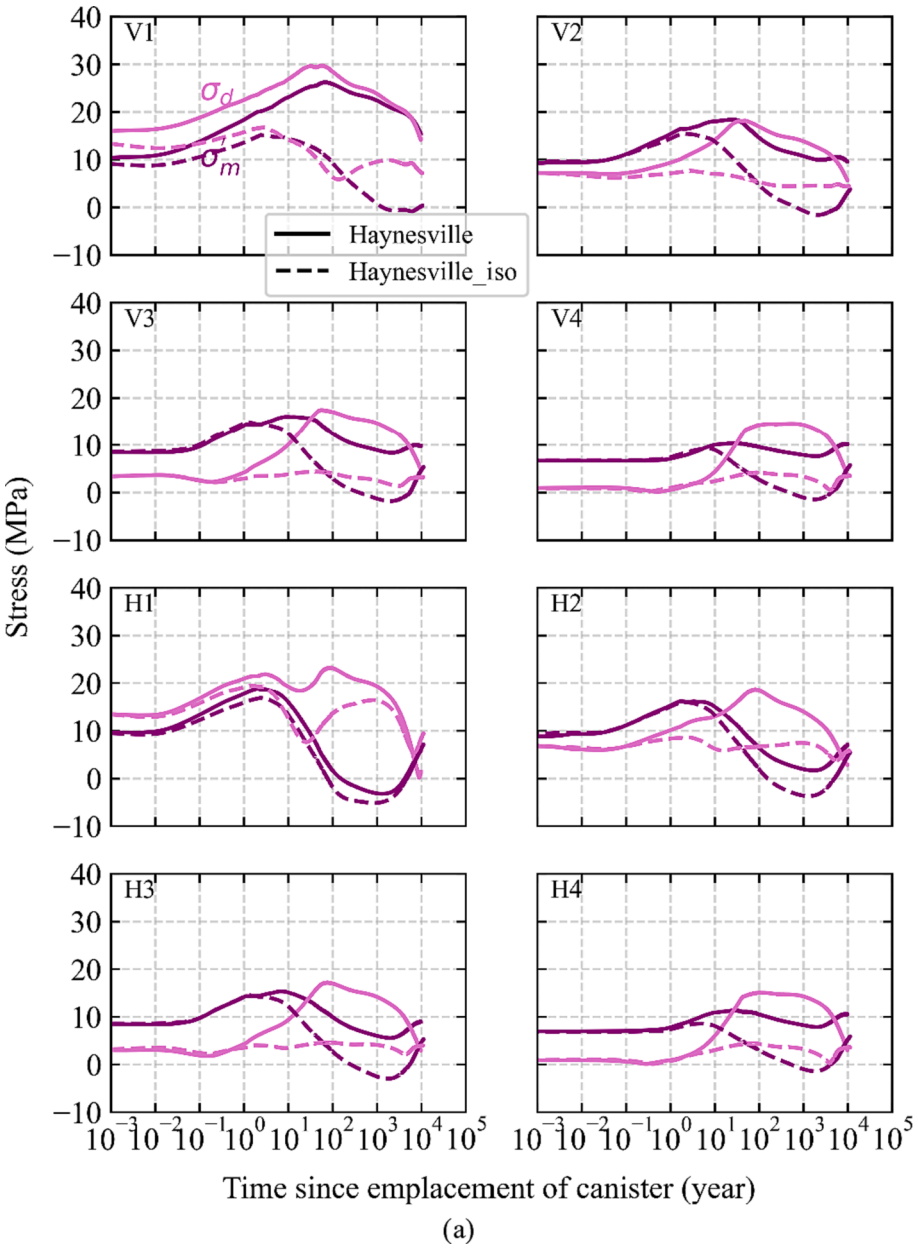

Fig. 12. The evolution of mean effective and deviatoric stresses at selected locations in the formation with (a) the Haynesville and (b) the Barnett shale properties (anisotropic creep vs. isotropic creep cases).

$$\left(d\dot{\epsilon}^{vp}_{L,ij}\right) = mA^{\frac{1}{m}}\left(\frac{\epsilon_{cr}+\epsilon_{shift}}{t_{ref}}\right)^{\frac{m-1}{m}}\left\langle\frac{f}{\sigma_{ref}}\right\rangle^{\left(\frac{n}{m}\right)}\begin{pmatrix}\frac{\partial f}{\partial\sigma'_{L,11}} & \frac{1}{2}\frac{\partial f}{\partial\sigma'_{L,12}} & \frac{1}{2}\frac{\partial f}{\partial\sigma'_{L,13}}\\ \frac{1}{2}\frac{\partial f}{\partial\sigma'_{L,12}} & \frac{\partial f}{\partial\sigma'_{L,22}} & \frac{1}{2}\frac{\partial f}{\partial\sigma'_{L,23}}\\ \frac{1}{2}\frac{\partial f}{\partial\sigma'_{L,13}} & \frac{1}{2}\frac{\partial f}{\partial\sigma'_{L,23}} & \frac{\partial f}{\partial\sigma'_{L,33}}\end{pmatrix} \tag{31}$$

where $\left(d\dot{\epsilon}^{vp}_{L,ij}\right)$ represents the components of the cross-anisotropic creep strain increment tensor,$d\dot{\boldsymbol{\epsilon}}^{vp}_{L}$ (-).

The creep strain increments in the local coordinates are then converted into those in the global coordinates as follows.

$$d\dot{\boldsymbol{\epsilon}}^{vp}_{G} = \boldsymbol{Q}^{T}\bullet d\dot{\boldsymbol{\epsilon}}^{vp}_{L}\bullet\boldsymbol{Q} \tag{32}$$

where $d\dot{\boldsymbol{\epsilon}}^{vp}_{G}$ (-) is the creep strain increment tensor in the global coordinates. Finally, stress increments are calculated using Hooke's law.

$$d\dot{\boldsymbol{\sigma}}_{\mathrm{G}} = \mathbb{C}_{A}\bullet\bullet\left(d\dot{\boldsymbol{\epsilon}}^{T}_{G} - d\dot{\boldsymbol{\epsilon}}^{vp}_{G} - d\dot{\boldsymbol{\epsilon}}^{th}_{G}\right) \tag{33}$$

where $\mathbb{C}_A$ (Pa) is the fourth-order tensor of cross-anisotropic elastic moduli, which have five independent components (i.e., Young's moduli and Poisson's ratios in the bedding parallel and bedding normal directions (E_P, E_N, ν_P, ν_N), and a shear modulus in the bedding normal direction (G_N)), $d\dot{\boldsymbol{\sigma}}_{\mathrm{G}}$ (Pa) is the effective stress increment tensor, $d\dot{\boldsymbol{\epsilon}}^{T}_{G}$ (-) is the total strain increment tensor, and $d\dot{\boldsymbol{\epsilon}}^{th}_{G}$ (-) is the thermal strain increment tensor, all of which are defined in the global coordinates. Note that the '$\bullet\bullet$' operator signifies double dot multiplication (e.g., $\boldsymbol{a}\otimes\boldsymbol{b}\bullet\bullet\boldsymbol{c}\otimes\boldsymbol{d} = (\boldsymbol{a}\bullet\boldsymbol{d})(\boldsymbol{b}\bullet\boldsymbol{c})$ where $\boldsymbol{a},\boldsymbol{b},\boldsymbol{c},\boldsymbol{d}$ are arbitrary vectors).

In shale creep, creep strain increments per unit time (i.e., creep strain

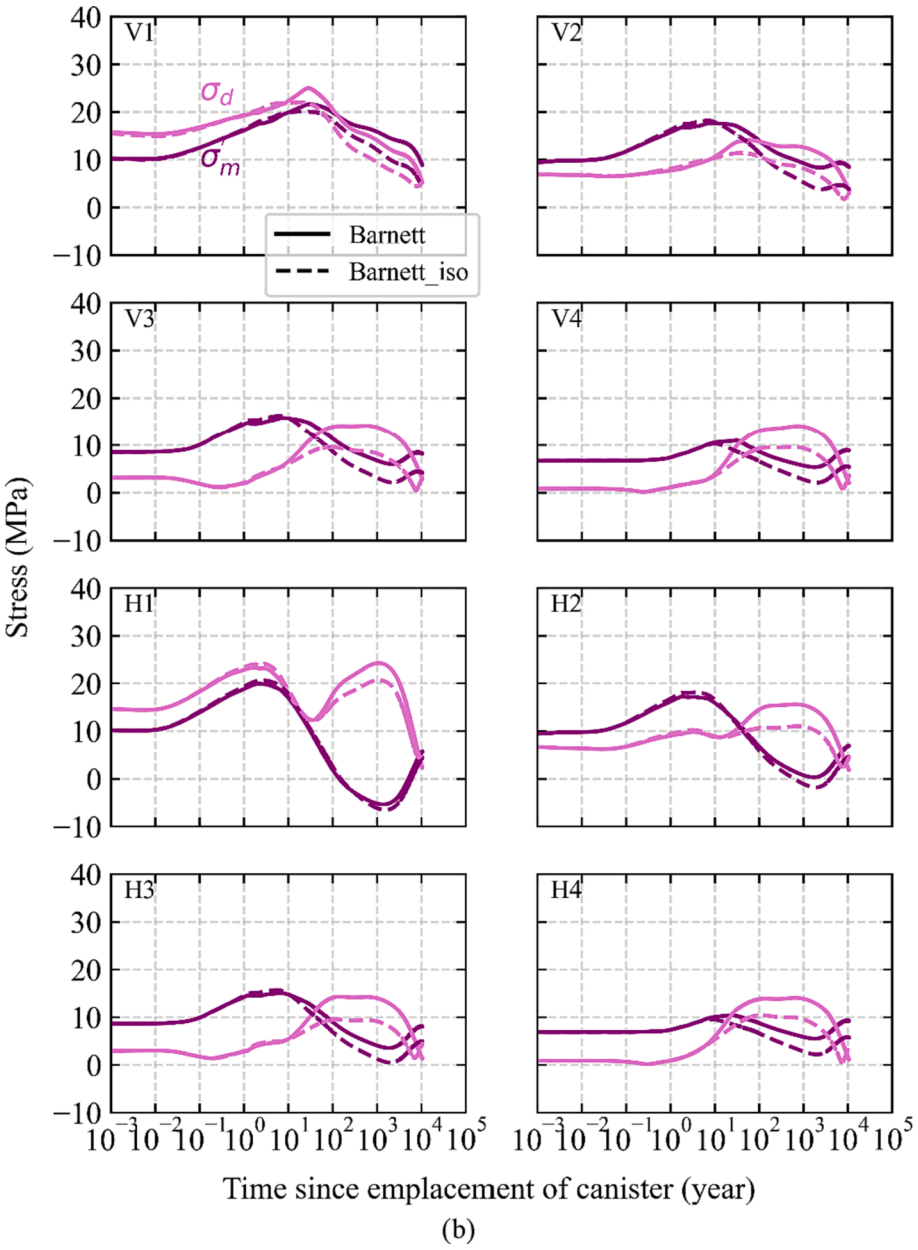

Fig. 12. (*continued*).

increment rates) decrease with increasing cumulative creep strains, which is often referred to as strain hardening. It is incorporated into the developed anisotropic creep model through increases in the ϵ_{cr} parameter:

$$d\dot{\epsilon}_{cr} = \sqrt{\frac{2}{3}\boldsymbol{d}\dot{\boldsymbol{\epsilon}}_L^{vp} : \boldsymbol{d}\dot{\boldsymbol{\epsilon}}_L^{vp}} + \left|\mathrm{tr}\left(\boldsymbol{d}\dot{\boldsymbol{\epsilon}}_L^{vp}\right)\right| \tag{34}$$

Also, the strain hardening of the Cam-Clay function is implemented via increases in the p_0 parameter:

$$d\dot{p}_0 = \frac{\nu p_0}{\lambda - \kappa}\left|\mathrm{tr}\left(\boldsymbol{d}\dot{\boldsymbol{\epsilon}}_L^{vp}\right)\right| \tag{35}$$

where ν (-) is the specific volume ($\nu = 1 + e = 1 + \phi/(1-\phi)$ where e (-) and ϕ (-) are the void ratio and porosity, respectively), and λ (-) and κ (-) are Cam-Clay parameters often referred to as the slope of compression and swelling lines, respectively. Note that the operator signifies taking the absolute value of what is inside of it. Also, note that the initial value of ϵ_{cr} is zero, whereas that of p_0 is nonzero, as the initial value of p_0 is related to the maximum compressive stress that formations have experienced.

2.3.1. Model parameter calibration

In order to calibrate the developed anisotropic creep model, a one-element simulation was carried out with the FLAC3D simulator. The simulation modelled the triaxial creep testing of shales in the laboratory (Sone & Zoback, 2013b) where shales retrieved from different formations in the US were subjected to axial loading under confining pressure. The testing duration was up to three hours, which might be too short to capture the long-term creep characteristics of shales. This testing provides, however, unique measurement data that few other experiments have: radial strain data for varied bedding directions. Such data are essential for the calibration of anisotropic creep models; hence, data from this testing was used.

Specifically, data for the 'Haynesville-1 V' and 'Barnett-1H' shales were selected, because these data were also used for the calibration of another anisotropic creep model (Borja et al., 2020). The Haynesville-1

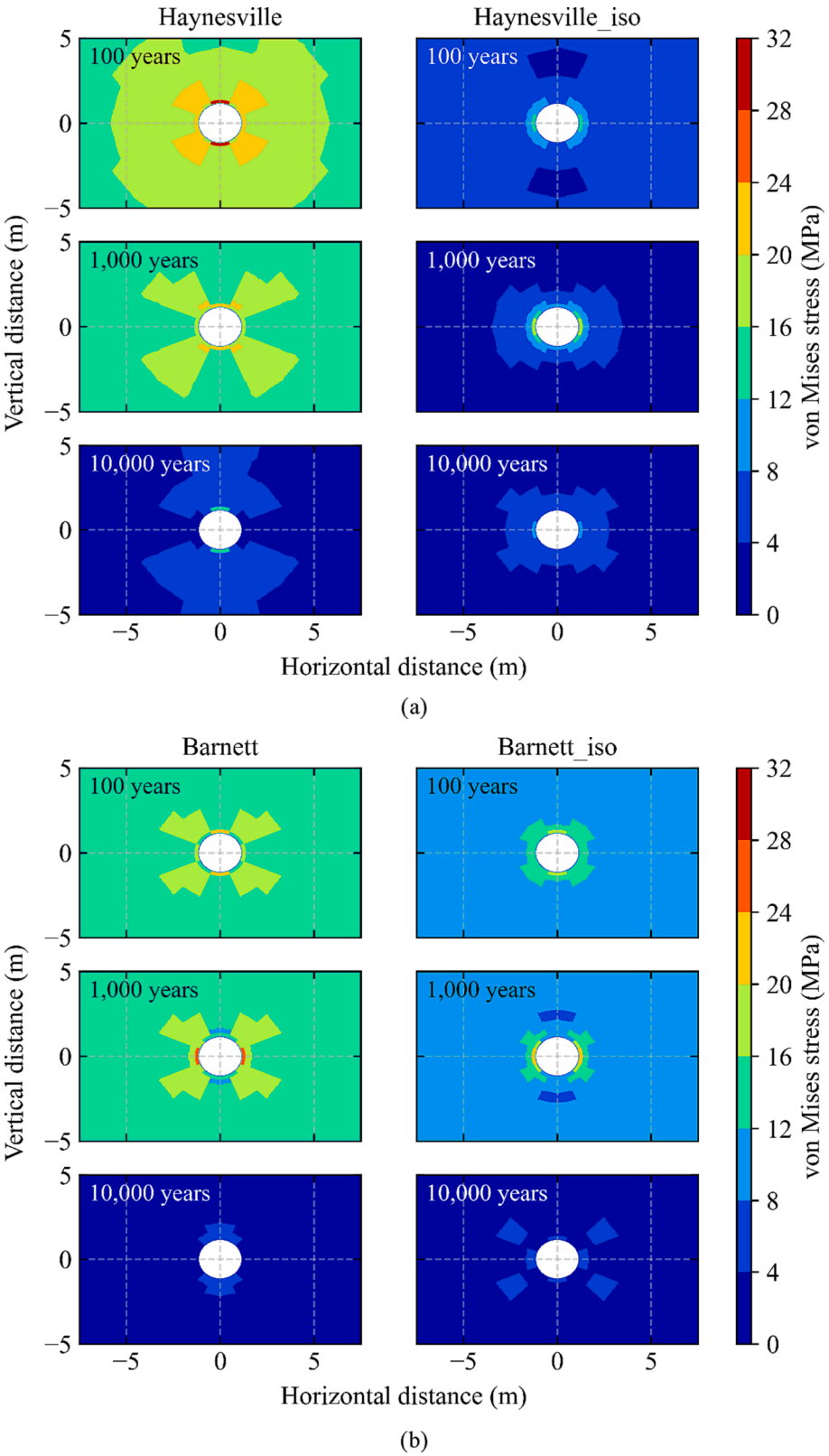

Fig. 13. Distributions of the deviatoric stress in the formation with (a) the Haynesville and (b) the Barnett shale properties (anisotropic creep vs. isotropic creep cases) at different times (100 vs. 1,000 vs. 10,000 years).

V shale was axially loaded in the direction normal to the bedding, while the Barnett-1H shale parallel to the bedding. The testing (and the corresponding modelling) procedures were as follows. First, confining pressures of 30 MPa and 20 MPa was applied (i.e., $\sigma_{11} = \sigma_{22} = \sigma_{33} = p_C$ and $\sigma_{12} = \sigma_{23} = \sigma_{13} = 0$ where p_C is the confining pressure) for the Haynesville-1 V and Barnett-1H shales, respectively; then, the axial stress was respectively increased by 29 MPa and 48 MPa (i.e., $\sigma_{33} = p_C + p_{diff}$ where p_{diff} is the axial stress increment). Note that pore

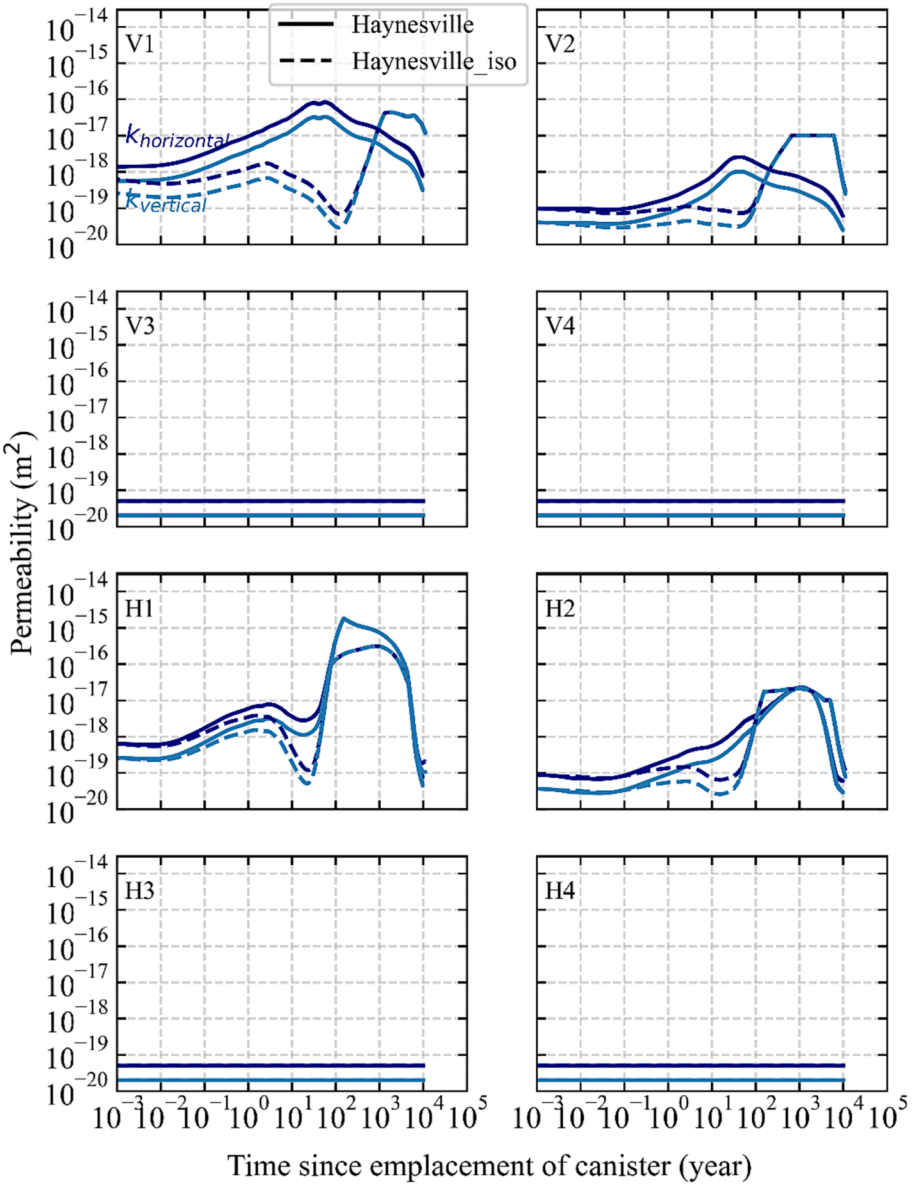

(a)

Fig. 14. The evolution of permeability at selected locations in the formation with(a) the Haynesville and (b) the Barnett shale properties (anisotropic creep vs. isotropic creep cases).

pressure was set to zero, and temperature was not considered in this simulation of the laboratory experiments, as the shales were room-dried before they were tested under room temperature and pressure conditions.

The cross-anisotropic mechanical (i.e., elastic and creep) properties and their values used in the simulation are listed in Table 4. The bedding angle (measured from a horizontal plane), β, was set to 0° and 90° for the Haynesville-1 V and Barnett-1H shales, respectively. Although it might seem that there were many parameters needing calibration, it was actually only four parameters (c_H, m, A, e_{shift}) that were calibrated. All the other parameter values were either simply set to unity (c_V, c_S, n, σ_{ref}, t_{ref}), or given relevant values from the initial condition (p_0) or from the literature (all the remaining parameters). Note that it was assumed in Eq. (35) that $(\lambda - \kappa) \approx \lambda$, as it is often the case that $\lambda \gg \kappa$ for most soils and rocks; also, the shear modulus was approximated by $G_N = E_N/(2(1+\nu_N))$.

Results of the calibration are shown in Fig. 3. The experimental data show that the axial creep strains of the Haynesville-1 V shale are much greater than those of the Barnett-1H shale, even though the axial differential stress was much greater in the latter than in the former shale (29 MPa vs. 48 MPa). This shows the effect of the loading direction being normal (Haynesville-1 V) or parallel (Barnett-1H) to the bedding, namely, shale accumulates a significantly greater amount of creep strains when loaded normal to the bedding. Note that the clay content of each shale was in the same range (36–39% in volume); also, the values of the elastic properties were in similar ranges (Sone & Zoback, 2013a). Hence, the effect of the bedding direction was substantial. This applies to the radial strains as well.

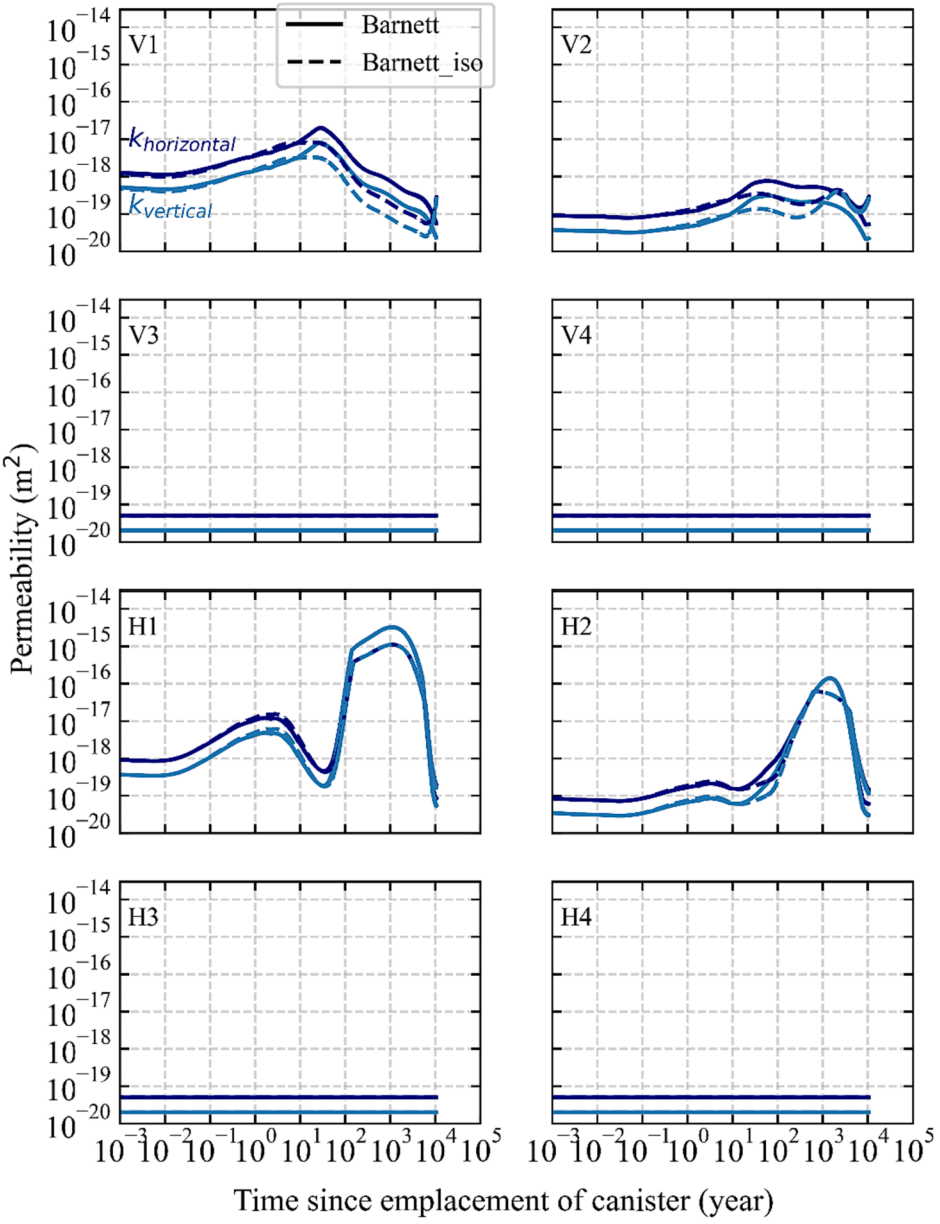

(b)

Fig. 14. (*continued*).

These trends in creep strains were captured by the numerical simulation. As it was not disclosed whether the radial strains of the Barnett-1H shale was measured in the bedding normal (BN) or parallel (BP) direction (Sone & Zoback, 2013b), numerical results show creep strains in both radial directions. It was found that the numerical radial strains in the BN direction were slightly greater than those in the BP direction, but this requires further validation as more experimental data become available. Also, note that, although the numerical radial strains of the Haynesville-1 V shale appear to match the experimental data, the numerical strains continue to grow, whereas the experimental data show no significant growth after about an hour. This might turn out to be true in longer-term testing (than this relatively short-term, three-hour testing). An upgrade of the developed model needs to be carried out if data from such longer-term testing shows the same trend, but for now, the current anisotropic creep model is sufficient to assess the effects of anisotropic shale creep on the behavior of a geological nuclear waste repository.

2.3.2. *Simulation of different shale creep cases*

Although the anisotropic creep model with the calibrated parameter values was able to capture the (short-term) creep testing results of the Haynesville-1 V and Barnett-1H shales, there are other testing results that show different creep characteristics. For example, shales with a large power-law coefficient (A) and a small power-law exponent (m) accumulated a lot of short-term creep but not so much in the long term. The opposite was true for shales with a small A and a large m (Benge et al., 2021). The Haynesville-1 V and Barnett-1H shales are more of the former type (i.e., short-term creep with a large A and small m); hence, the long-term effect might be limited in the selected two shales. As such, long-term creep versions of the Haynesvill-1 V and Barnett-1B shales

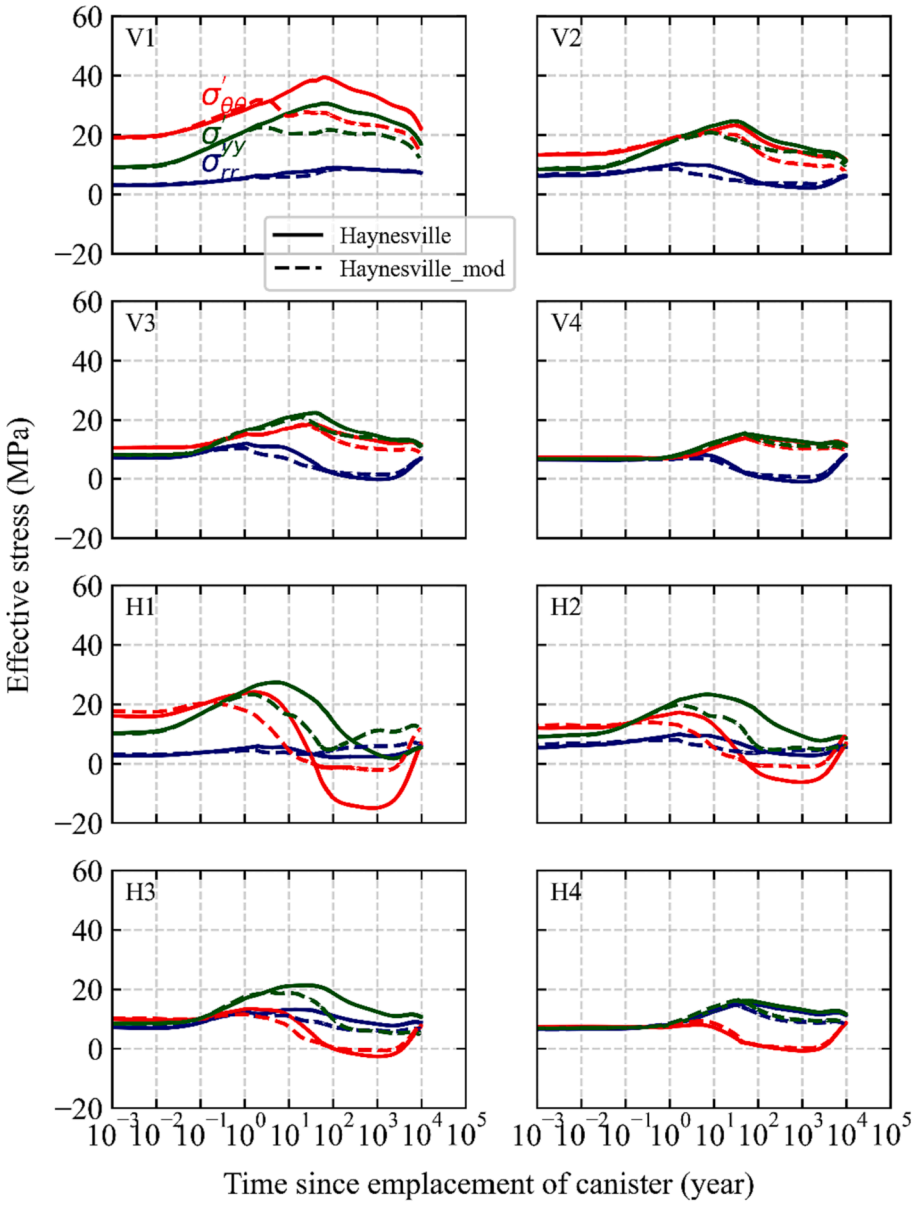

(a)

Fig. 15. The evolution of stresses at selected locations in the formation with the Haynesville shale properties (short-term creep vs. long-term creep cases): (a) effective stress; (b) mean effective and deviatoric stresses.

were created by assigning power-law coefficient and exponent values based on those of Caney Shale examined by Benge et al. (2021). Note that precise calibration of the anisotropic creep model was not feasible for Caney Shale, as only axial strain data are available in Benge et al. (2021).

In addition to simulating the long-term creep, it was also necessary to simulate isotropic creep versions of the Haynesville-1 V and Barnett-1H shales so that the effect of anisotropic creep could be clarified. Isotropic creep versions of the two shales were created by ignoring the anisotropic stress tensor (i.e., by using the original Cauchy stress tensor) and also by ignoring the Cam-Clay parameters.

The parameter values for the long-term and isotropic shale creep cases are provided in Table 5 and Table 6. Only those parameters that were modified for creating each case are listed in the tables (i.e., the remaining parameter values are the same as those in Table 4).

Fig. 4 shows axial creep strains developed in the long-term and isotropic creep cases in comparison with the original, calibrated anisotropic creep case. Note that the creep compliance is defined as the axial creep strain (i.e., creep strain in the z-axis direction in Fig. 2) divided by the applied differential stress; also, this simulation is identical to the calibration simulation except for the modified parameter values listed in Table 5 and Table 6. It is shown that, compared to the calibrated anisotropic case, the long-term creep case ("Haynesville_mod" & "Barnett_mod") develops much less creep strains in the short term. It develops, however, much greater creep strains in the long term. The isotropic case ("Haynesville_iso" & "Barnett_iso"), on the other hand, might appear nearly identical to the original anisotropic case. That is true except for the isotropic case ignoring the bedding direction and

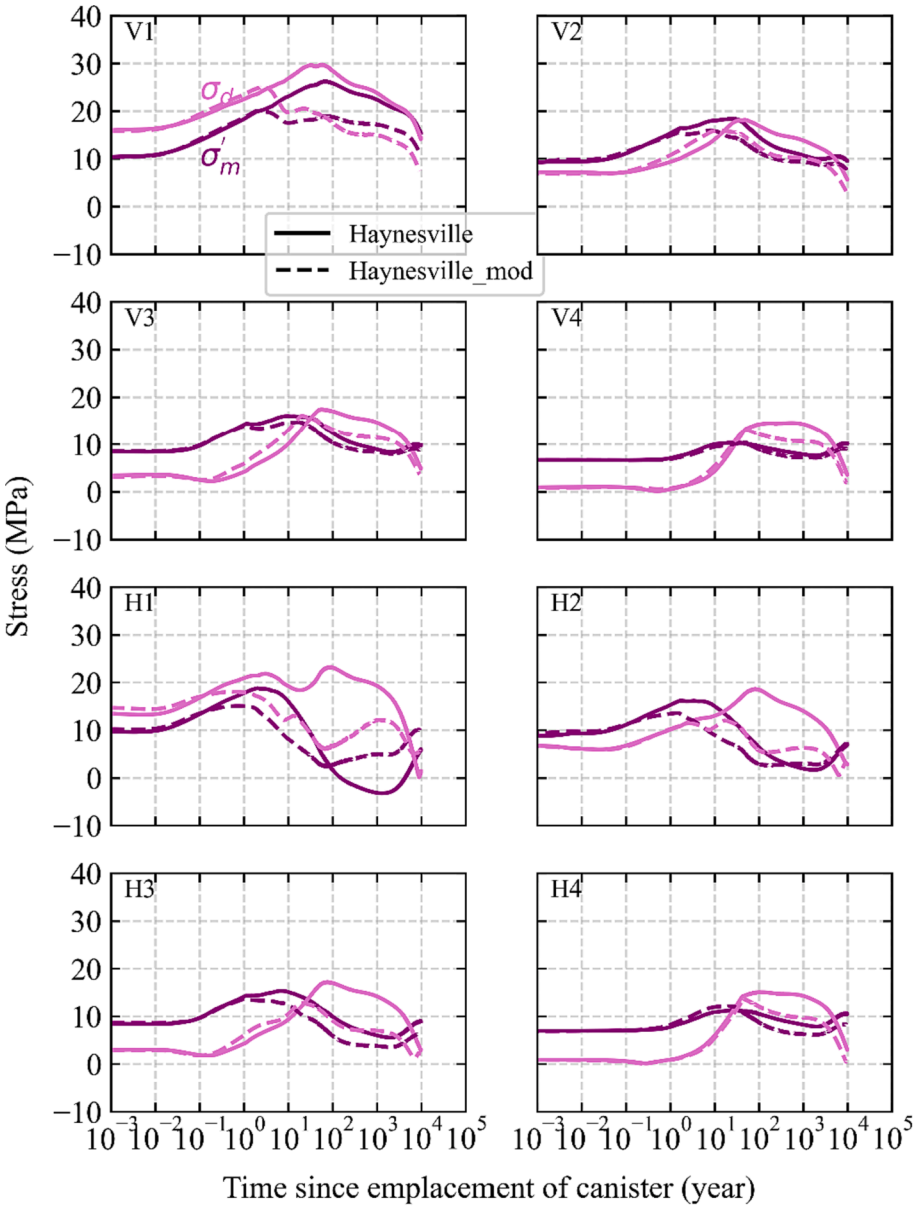

(b)

Fig. 15. (*continued*).

developing zero volumetric creep strains, which are not captured in Fig. 4.

In the simulation of the repository, a comparison between the anisotropic and isotropic creep cases will show the effects of more precise, realistic modelling of shale creep vs. approximate, simplified modelling of shale creep, whereas a comparison between the short-term and long-term anisotropic creep cases will literally show the effects of short-term vs. long-term shale creep, on the behavior of the repository.

2.4. Modelling steps

2.4.1. Initial state

In the initial state, the repository model was assumed to consist only of the rock (shale formation) (i.e., the drift is not excavated yet). The initial THM state was set by calculating TH equilibrium in TOUGH3 and M equilibrium in FLAC3D with the boundary conditions and parameter values previously shown in Fig. 1 and Table 1, respectively. As a result, constant vertical gradients of temperature (0.03 (^{o}C/m)), pore pressure (9.81 (kPa/m)), and total stresses (24.0 (kPa/m)) were achieved. The initial stress state was isotropic, namely, the stresses in the vertical and horizontal directions were equal to one another.

2.4.2. Drift excavation

Following the initial state, the rock zones inside of the drift area were removed while simultaneously a constant temperature, pore pressure, and surface pressure of 25 °C, 0.1 MPa, and 0.1 MPa were applied to the drift's boundary surface, respectively, to initiate the drift excavation stage. In this stage, in which the simulated duration was 1.5 years, TOUGH3 and FLAC3D were coupled (i.e., TOUGH-FLAC) to simulate the THM-coupled behavior of the repository. Note that the rock was assumed to be anisotropic elastic during this stage (i.e., no creep). Also, the failure of shale, especially the EDZ, was not considered in this study,

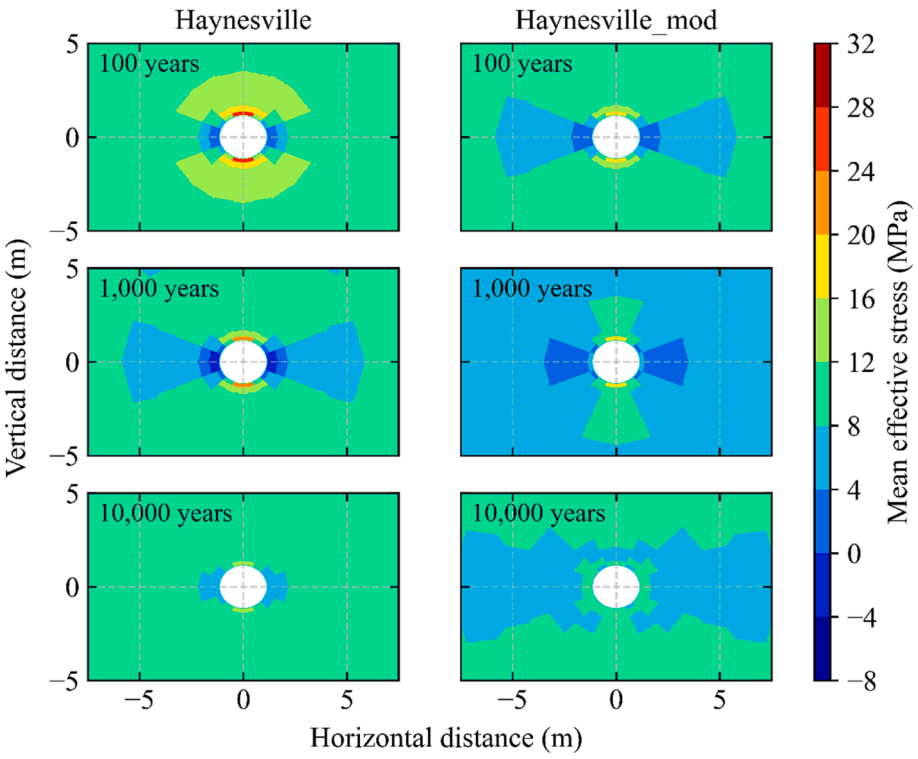

Fig. 16. Distributions of the mean effective stress in the formation with the Haynesville shale properties (short-term creep vs. long-term creep cases) at different times (100 vs. 1,000 vs. 10,000 years).

which should have had tangible impacts on the stress field following the excavation. This is a limitation of this study.

2.4.3. Post-closure

After the 1.5-year excavation stage, the canister and bentonite zones were activated inside of the drift and their initial temperature, pore pressure, and total stresses were set to 25 °C, 0.1 MPa, and 0.2 MPa, respectively; also, an initial gas-phase saturation of 0.35 was assigned, which generated corresponding initial capillary pressure according to Eq. (8). Moreover, the preconsolidation pressure, p_0, of the anisotropic creep model was given the values equal to the mean effective stress values ($= \mathrm{tr}(\boldsymbol{\sigma}')/3$) of the formation at each depth (i.e., p_0 was depth-varying). Note that other parameters were assumed to be constant along the depth, which might have some impacts on the modelling results. To simulate the decay heating of nuclear waste, the time-varying heat source shown in Fig. 5 was assigned to each of the sixteen canister zones that form the outer surface of the canister. The combined heat sources represent nuclear waste packages each of which contains four PWR (pressurized water reactor) spent fuels after 60 years of interim storage placed at a center-to-center spacing of 9 m in the drift's axis direction.

3. Results

Results of the post-closure stage of the simulation were extracted from selected locations in the formation as shown in Fig. 6 for analysis and comparison, which were made between three different cases: anisotropic creep vs. no creep (i.e., anisotropic elastic) cases; anisotropic creep vs. isotropic creep cases; and anisotropic short-term creep vs. anisotropic long-term creep cases. Each comparison was aimed at providing insights into the effects of anisotropic shale creep on the performance of the repository.

3.1. Anisotropic creep vs. no creep cases

3.1.1. Temperature, pore pressure, and saturation

Fig. 7a shows the evolution of temperature, pore pressure, and liquid-phase saturation at the selected locations in the formation with the Haynesville-1 V shale properties, while Fig. 7b shows the results corresponding to the Barnett-1H shale properties. Temperatures increased rather gradually and a peak of slightly less than 80 °C was computed near the drift wall (at V1, H1) toward 100 years since the closure of the drift. Temperature peaks at the other locations occurred with some delay in proportion to the distance from the drift. Pore pressure, on the other hand, remained at near zero values in early periods before it increased abruptly to a peak of approximately 16 MPa slightly after 1,000 years. This is because the formation was not fully saturated near the drift in early periods while the gas initially trapped in the bentonite continued to escape into the formation. Also, it was found that there was no delay in pore pressure peaks. The synchronized pore pressure peaks were driven by fluid flow; as soon as local pore pressure peaks developed due to thermal pressurization, they dissipated via fluid flow to an average (common) pore pressure level in the respective region of the formation. Had fluid flow been restricted, for example, by setting the permeability of the formation to zero, delayed pore pressure peaks would have appeared just as the delayed temperature peaks did.

Both Fig. 7a and b show that it was only for pore pressure that any difference was found between the anisotropic creep and no creep cases. The anisotropic creep case resulted in pore pressure peaks of less magnitude than the no creep case. For example, the difference was as much as 3.5 MPa and 1 MPa (at about 1,000 years) in the formation with the Haynesville and Barnett shale properties, respectively. The reduced pore pressure was caused by creep-induced stress relaxation in the formation, especially near the drift, i.e., creep strains decrease elastic strains as shown earlier in Eq. (33), leading to reduced effective stresses near the drift, which in turn helps to relax broader areas of the formation. Such stress relaxation expanded the pore volume of the formation; as a result, pore pressure decreased. The pore pressure reduction was

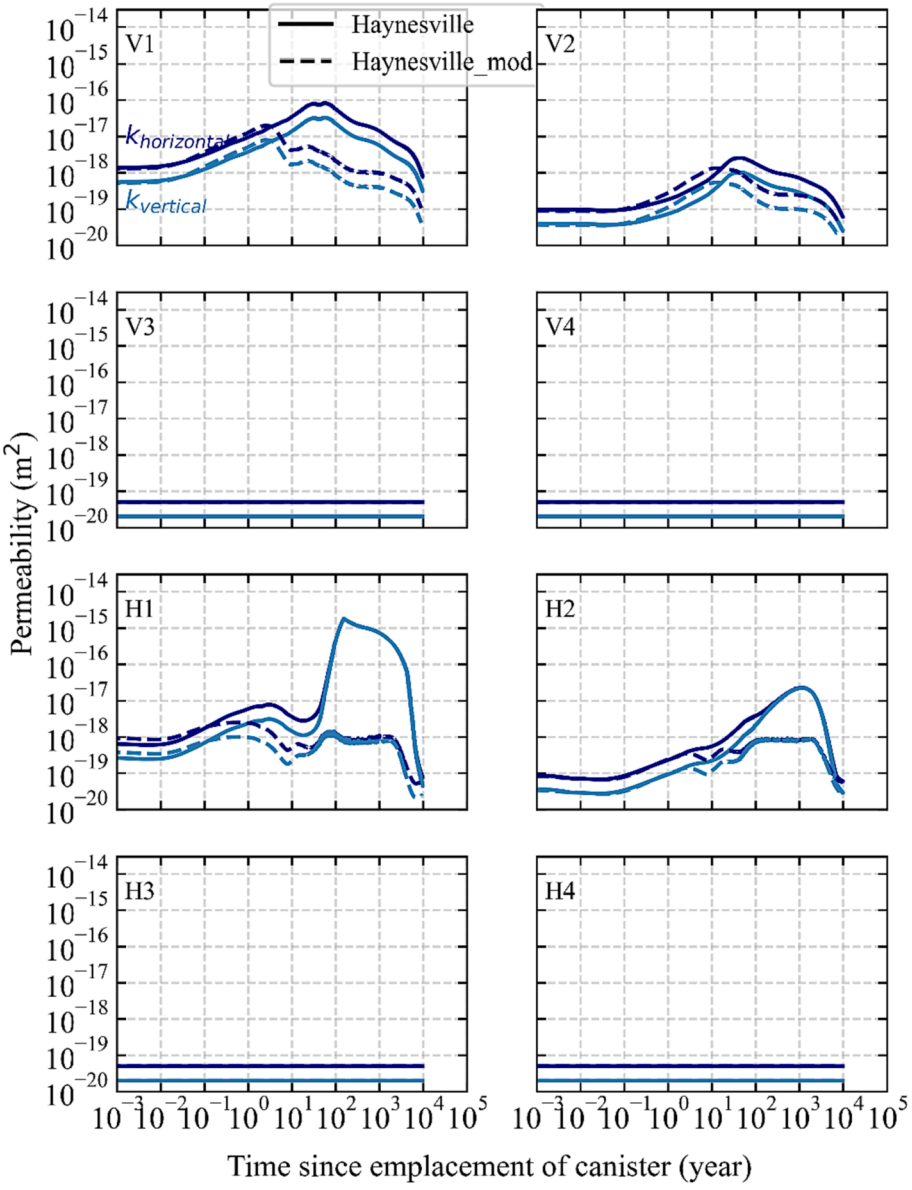

Fig. 17. The evolution of permeability at selected locations in the formation with the Haynesville shale properties (short-term creep vs. long-term creep cases).

greater in the formation with the Haynesville shale properties than that with the Barnett shale properties, as the former shale developed greater creep strains than the latter shale.

It is noted that although anisotropic shale creep affected the pore pressure development, the effect was relatively minor (and it was nonexistent in the temperature and saturation development). Also, it is not pore pressure that compromises formations mechanically; it is the effective stress that matters. Hence, in this and the other comparison cases, results for temperature, pore pressure, and saturation are omitted, and instead, the results are focused on stresses and permeability.

3.1.2. Stresses

Fig. 8 shows the evolution of total, mean effective, and deviatoric stresses in the formation with the Haynesville shale properties. Results for the Barnett shale properties are omitted because only similar trends were identified. The general trend in terms of total stress was that it increased with increasing temperature and pore pressure at the vertical locations (V1-4), whereas circumferential total stress decreased to or below zero at the horizontal locations (H1-4). This is because tensile strains were generated at these locations, as the drift deformed in an ellipsoidal shape (where the minor axis is aligned with the horizontal plane) due to the lateral boundary displacement constraint. Note that positive stress values indicate compression, and negative values tension.

A comparison between the anisotropic creep and no creep cases shows that the effect of creep was to decrease total, mean effective, and deviatoric stresses. This was the case regardless of the directions of stress (e.g., $\sigma_{rr}, \sigma_{\theta\theta}, \sigma_{yy}$), locations in the formation (i.e., V1-4, H1-4) or shale types (i.e., Haynesville, Barnett). This indicates that simulations with elastic (i.e., no creep) constitutive models for the formation would consistently overestimate stress levels relative to more realistic simulation cases where creep is considered. This claim is corroborated with the contours of deviatoric stress shown in Fig. 9.

A remark on the total stress evolution: in a longer term (>10,000 years), total stress levels are expected to converge toward overburden stress levels; since vertical total stress levels are essentially constant (i.e., the self-weight of the formation), horizontal total stress levels should approach them as creep strains continue to develop. Note that this might not be true near the drift (e.g., V1, H1), because total vertical stress levels are disturbed by drift excavation, and they might thus not approach values specified by the self-weight of the formation.

3.1.3. Permeability

Fig. 10 shows the evolution of permeability in the formation with the Haynesville shale properties. Because similar results were obtained in the results for the Barnett shale properties, they are omitted. Note that permeability values differed between the anisotropic creep and no creep cases only at the V1, V2, H1, and H2 locations, since they were located inside of the EDZ where permeability was assumed to follow the empirical function (Eq. (19)). The general trend was found to be similar to that of the stresses, i.e., permeability values peaked between approximately 100 and 1,000 years. The largest permeability value was over 10^{-15} m^2 at the H1 location, where mean effective stress was small and deviatoric stress was large, reflecting the tendency of such stress conditions to open and/or generate fractures.

A comparison between the anisotropic creep and no creep cases shows that the no creep case overestimated permeability levels at vertical locations (V1, V2) while it underestimated permeability values at a horizontal location (H2). Permeability values at the H1 location did not differ much between the two cases. Although not shown here for brevity, a consistent trend (i.e., the overestimation of permeability levels at vertical locations in the no creep case) was found in Barnett shale results; thus, that is the insight obtained from this comparison. Note, however, that the permeability values provided in Fig. 10 were estimated from the particular permeability model (Eq. (19)); had another permeability model been used, estimated permeability levels could have been significantly different. Also, the failure of shale and the corresponding permeability change were not considered in this study; had they been considered, the permeability levels should have changed not only within the EDZ but also outside of it (i.e., V3, V4, H3, H4). Hence, the above finding is dependent on the validity of the permeability model and the omission of shale failure, although it does anyway indicate that creep has a significant impact on the permeability evolution in the EDZ.

3.1.4. Stresses in the bentonite buffer

Fig. 11 shows the evolution of mean total and effective stresses in the bentonite buffer extracted at the middle radius of the bentonite along the vertical axis. Results differed only in total stress between the two cases, which was due to the difference in pore pressure explained earlier (Fig. 7). The effective stress levels were identical (the solid and dashed lines are on top of each other) not only between the two cases but also between the cases with different shale types (not shown here for brevity), indicating that shale creep would not affect the evolution of effective stress in the bentonite buffer. However, the outcome could be attributed to the simple linear elasticity (and linear swelling) employed for the bentonite. Use of more elaborate constitutive models might have produced different results.

It is noted that because the same results were obtained in terms of mean effective stress in the bentonite in the other comparison cases, they are not shown in the following sections.

3.2. Anisotropic creep vs. isotropic creep cases

In this comparison, only results for certain types of stress (and permeability) are provided, as results for the other stress measures were found not to be the essence of the comparison.

3.2.1. Stresses

Fig. 12a and b show the evolution of mean effective and deviatoric stresses in the formation with the Haynesville and Barnet shale properties, respectively. They show that the isotropic creep case consistently underestimated (compressive) stress levels relative to the anisotropic creep case. Especially, in the Haynesville shale results at the V1 location at approximately 1,000 years, a mean effective stress of 0 MPa was reached in the isotropic case, whereas a mean effective stress of over 20 MPa was still sustained in the anisotropic case. Although an extreme example, it indicates the trend that isotropic shale creep could (significantly) underestimate stress levels in the formation around the drifts of a geological nuclear waste repository during the post-closure period. This seems, however, dependent on shale types, as the underestimation of stresses was much less in the Barnett shale formation. These claims are also supported by the contours of deviatoric stress shown in Fig. 13.

3.2.2. Permeability

Fig. 14a and b show the evolution of permeability in the formation with the Haynesville and Barnet shale properties, respectively. The general trend is that permeability values in the isotropic creep case were significantly underestimated relative to those in the anisotropic creep case, which is a direct result of the stress underestimation discussed earlier. This could fictitiously indicate a favorable performance of the repository. Some permeability values were, however, higher in the isotropic creep case at certain locations at certain times. For example, at the V1 and V2 locations between 1,000 and 1,000 years in the Haynesville shale results, permeability values in the isotropic creep case were greater by roughly an order of magnitude. This was because mean effective stress levels decreased to zero or negative values in the isotropic creep case, which significantly increased permeability values according to Eq. (19) by reflecting potential fracture opening. Although such an outcome was dependent on the particular permeability function, zero or tensile mean effective stress levels should certainly increase permeability levels regardless of the choice of permeability functions. Hence, the overestimation of permeability increases in the long term (>1,000 years), which is equivalent to predicting a fictitiously less favorable performance of the repository, would be another (minor) shortcoming of using an isotropic creep constitutive model.

3.3. Short-term creep vs. long-term creep cases

In this comparison, only results for the Haynesville shale properties are provided, because similar trends were obtained from results for the Barnett shale properties. The essence of this comparison is to provide an insight into whether shale formations with short- or long-term creep characteristics are more beneficial for the repository performance.

3.3.1. Stresses

Fig. 15a and b show the evolution of effective, mean effective, and deviatoric stresses, respectively. It was found that the long-term creep case (i.e., shown as “Haynesville_mod” in the figure legends) not only resulted in smaller (compressive) stress levels but also prevented large tensile effective stresses from developing at horizontal locations. For example, at the H1 location in the short-term creep case, a tensile circumferential effective stress of over 15 MPa was generated at 1,000 years, whereas it was just 1–2 MPa in the long-term creep case. Although not shown, this was also the case in the Barnett shale formation. Also, due to the significant reduction in tensile stress, mean effective stress levels consistently remained compressive (i.e., above zeros) in the long-term creep case, with the smallest values being at least 2–3 MPa throughout the simulated post-closure period. This is also supported by the effective stress contours shown in Fig. 16. A large drop in tensile effective stress and maintained compressive mean effective stress levels should in general lead to a significantly increase in the performance of a geological nuclear waste repository by preventing potential generation and opening of fractures.

3.3.2. Permeability

Fig. 17 shows the evolution of permeability in the formation with the Haynesville shale properties. Since mean effective stress levels remained compressive, the large increases in permeability previously shown in the anisotropic (short-term) and isotropic creep cases at the V1 and H1 locations did not repeat themselves in the anisotropic long-term creep case. As a result, permeability values significantly decreased relative to the short-term creep case by, for example, three orders of magnitude at the H1 location at roughly 100 years. This indicates the potential of shales with the long-term creep characteristics, namely, a large creep

exponent value (e.g., $m = 0.16$ and 0.60 for the short- and long-term creep cases, respectively), to achieve strong long-term performance as part of the barrier system of a geological nuclear waste repository. Although, such an insight would only be valid if the choice of permeability functions was appropriate, it does not change the fact that the long-term creep case resulted in consistently lower deviatoric stress levels while maintaining compressive mean effective stress levels as discussed earlier. This should lead to significant decreases in permeability relative to the short-term creep case even if different permeability functions are employed. Hence, it is argued that shales with the long-term creep characteristics would be suitable for hosting a geological nuclear waste repository from the perspectives of its long-term safety and performance.

4. Conclusions

In this research, thermo-hydromechanically (THM) coupled simulations of a generic geological nuclear waste repository were carried out with an anisotropic creep constitutive model for shale. The objective was to compare the long-term stress and permeability evolution of the repository among different shale creep cases, such as no creep (i.e., elastic), isotropic creep, and long-term creep shale cases, in order to better understand the effects of anisotropic shale creep on the performance of a geological nuclear waste repository. Results of this research provided the following insights:

- The no creep (i.e., elastic) shale creep case overestimated stress levels in the formation by as much as 10 MPa between 100 and 1,000 years in the post-closure period, which resulted in overestimated increases in permeability. Hence, simulations with an elastic formation model will lead to conservative performance assessment of geological nuclear waste repositories.
- The isotropic creep shale case underestimated stress levels but the magnitudes of underestimation were dependent on shale types (e.g., Haynesville vs. Barnett). Permeability levels were also underestimated at early times of the post-closure period (e.g., before 100 years), but they were significantly overestimated by roughly an order of magnitude at later times (e.g., after 100 years) where mean effective stress levels decreased to zero or negative (i.e. tensile) values. This indicates that simulations with an isotropic creep formation model could provide inaccurate estimates of permeability evolution, and hence, an inaccurate performance assessment of geological nuclear waste repositories.
- In the long-term creep shale case, tensile stress did not develop in the formation while deviatoric and mean effective stress levels respectively decreased and remained compressive, which were all beneficial for the performance of the repository, because under such stress conditions permeability levels consistently remained low. A long-term creep shale is characterized by a large value of the power-low exponent (denoted as m in this research), and hence such shale would be favorable for hosting a geological nuclear waste repository.

In this research, permeability levels were estimated from stress levels via an empirical permeability function. In order to estimate more accurate permeability evolution, however, many other effects than just stress need to be considered, such as creep- and chemically-induced fracture healing, damage- and failure-induced fracture development, etc. Also, not considered was shale failure, which should have had tangible impacts on the stress and permeability evolution of the modelled shale repository. Such aspects may be addressed in the future research.

CRediT authorship contribution statement

Tsubasa Sasaki: Methodology, Software, Validation, Formal analysis, Investigation, Data curation, Writing – original draft, Writing – review & editing, Visualization. **Jonny Rutqvist:** Conceptualization, Software, Resources, Writing – review & editing, Supervision, Project administration, Funding acquisition.

Declaration of competing interest

The authors declare that they have no known competing financial interests or personal relationships that could have appeared to influence the work reported in this paper.

Data availability

Data will be made available on request.

Acknowledgements

Funding was provided by the Spent Fuel and Waste Science and Technology, Office of Nuclear Energy, of the U.S. Department of Energy under Contract Number DE-AC02-05CH11231 with Lawrence Berkeley National Laboratory.

References

Apted, M., Ahn, J., 2010. Geological Repository Systems for Safe Disposal of Spent Nuclear Fuels and Radioactive Waste, first ed. Woodhead Publishing.
Bailey, R.W., 1935. The utilization of creep test data in engineering design. Proc. Inst. Mech. Engineers 131 (1), 131–349. https://doi.org/10.1243/pime_proc_1935_131_012_02.
Barla, G., Debernardi, D., Sterpi, D., 2012. Time-Dependent modeling of tunnels in squeezing conditions. Int. J. Geomech. 12 (6), 697–710. https://doi.org/10.1061/(asce)gm.1943-5622.0000163.
Bechthold, W., Rothfuchs, T., Poley, A., Ghoreychi, M., Heusermann, S., Gens, A., Olivella, S., 1999. Backfilling and sealing of underground repositories for radioactive waste in salt (BAMBUS Project). https://op.europa.eu/en/publication-detail/-/publication/49ae90df-e3a6-4bd5-b55e-e505a9a15753.
Benge, M., Lu, Y., Katende, A., Rutqvist, J., Crandall, D., Haecker, A., King, G., Joseph, B., Radonjic, M., Bunger, A., Berkeley, L., Energy, N., Resources, C., Engineering, G.E.K., 2021. Connecting Geomechanical Properties with Potential for Proppant Embedment and Production Decline for the Emerging Caney Shale, Oklahoma. In: Unconventional Resources Technology Conference. https://doi.org/10.15530/urtec-2021-1234.
Blanco-Martín, L., Rutqvist, J., Birkholzer, J.T., 2015a. Long-term modeling of the thermal-hydraulic-mechanical response of a generic salt repository for heat-generating nuclear waste. Eng. Geol. 193, 198–211. https://doi.org/10.1016/j.enggeo.2015.04.014.
Blanco-Martín, L., Wolters, R., Rutqvist, J., Lux, K.H., Birkholzer, J.T., 2015b. Comparison of two simulators to investigate thermal-hydraulic-mechanical processes related to nuclear waste isolation in saliferous formations. Comput. Geotech. 66, 219–229. https://doi.org/10.1016/j.compgeo.2015.01.021.
Blanco-Martín, L., Rutqvist, J., Battistelli, A., Birkholzer, J.T., 2018. Coupled processes modeling in rock salt and crushed salt including halite solubility constraints: application to disposal of heat-generating nuclear waste. Transp. Porous Media 124 (1), 159–182. https://doi.org/10.1007/s11242-018-1057-7.
Blümling, P., Bernier, F., Lebon, P., Derek Martin, C., 2007. The excavation damaged zone in clay formations time-dependent behaviour and influence on performance assessment. Phys. Chem. Earth 32, 588–599. https://doi.org/10.1016/j.pce.2006.04.034.
Borja, R.I., Yin, Q., Zhao, Y., 2020. Cam-Clay plasticity. Part IX: On the anisotropy, heterogeneity, and viscoplasticity of shale. Comput. Methods Appl. Mech. Eng. 360 https://doi.org/10.1016/j.cma.2019.112695.
Bossart, P., Meier, P.M., Moeri, A., Trick, T., Mayor, J.C., 2002. Geological and hydraulic characterisation of the excavation disturbed zone in the Opalinus Clay of the Mont Terri Rock Laboratory. Eng. Geol. 66 (1–2), 19–38. https://doi.org/10.1016/S0013-7952(01)00140-5.
Chang, C., Zoback, M.D., 2009. Viscous creep in room-dried unconsolidated Gulf of Mexico shale (I): Experimental results. J. Pet. Sci. Eng. 69 (3–4), 239–246. https://doi.org/10.1016/j.petrol.2009.08.018.
Chang, C., Zoback, M.D., 2010. Viscous creep in room-dried unconsolidated Gulf of Mexico shale (II): development of a viscoplasticity model. J. Pet. Sci. Eng. 72 (1–2), 50–55. https://doi.org/10.1016/j.petrol.2010.03.002.
Cheng, A.H.D., 1997. Material coefficients of anisotropic poroelasticity. Int. J. Rock Mech. Mining Sci. Geomechanics Abstracts 34 (2), 199–205. https://doi.org/10.1016/S0148-9062(96)00055-1.
Choo, J., Semnani, S.J., White, J.A., Sone, H., 2021. Anisotropic creep in shale gas reservoir rocks: Impacts of constitutive behavior on field-scale deformations. In: 55th U.S. Rock Mechanics/Geomechanics Symposium 2021, 4.
Conil, N., Vitel, M., Plua, C., Vu, M.N., Seyedi, D., Armand, G., 2020. In situ investigation of the THM behavior of the Callovo-Oxfordian Claystone. Rock Mech. Rock Eng. 53 (6), 2747–2769. https://doi.org/10.1007/s00603-020-02073-8.

Duvaut, G., Lions, J.L, 1976. Inequalities in Mechanics and Physics. In Grundlehren Der Mathematischen Wissenschaften. https://doi.org/10.1007/978-3-642-66165-5.
IAEA, 2003. Scientific and Technical Basis for the Geological Disposal of Radioactive Wastes. https://www.iaea.org/publications/6568/scientific-and-technical-basis-for-the-geological-disposal-of-radioactive-wastes.
Jung, S., Vu, M.N., Pouya, A., Ghabezloo, S., 2022. Effect of anisotropic creep on the convergence of deep drifts in Callovo-Oxfordian claystone. Comput. Geotech. 152 (August), 105010 https://doi.org/10.1016/j.compgeo.2022.105010.
Kim, J., Tchelepi, H.A., Juanes, R., 2011. Stability and convergence of sequential methods for coupled flow and geomechanics: drained and undrained splits. Comput. Methods Appl. Mech. Eng. 200 (23–24), 2094–2116. https://doi.org/10.1016/j.cma.2011.02.011.
Kim, J., Moridis, G.J., Yang, D., Rutqvist, J., 2012a. Numerical studies on two-way coupled fluid flow and geomechanics in hydrate deposits. SPE J. 17 (2), 485–501. https://doi.org/10.2118/141304-PA.
Kim, J., Sonnenthal, E.L., Rutqvist, J., 2012b. Formulation and sequential numerical algorithms of coupled fluid/heat flow and geomechanics for multiple porosity materials. Int. J. Numer. Meth. Eng. 92, 425–456. https://doi.org/10.1002/nme.4340.
Lemaitre, J., 1979. Lemaitre_damage modelling.pdf. In: Transactions of the International Conference on Structural Mechanics in Reactor Technology: Vol. L.
Li, Y., Ghassemi, A., 2012. Creep behavior of Barnett, Haynesville, and Marcellus shale. In: 46th US Rock Mechanics/Geomechanics Symposium, 641–647. https://onepetro.org/ARMAUSRMS/proceedings-abstract/ARMA12/All-ARMA12/ARMA-2012-330/120741.
Mánica, M., Gens, A., Vaunat, J., Ruiz, D.F., 2016. A cross-anisotropic formulation for elasto-plastic models. Géotechnique Letters 6, 156–162. https://doi.org/10.1680/jgele.15.00182 A.
Mánica, M., Gens, A., Vaunat, J., Ruiz, D.F., 2017. A time-dependent anisotropic model for argillaceous rocks. Application to an underground excavation in Callovo-Oxfordian claystone. Comput. Geotech. 85, 341–350. https://doi.org/10.1016/j.compgeo.2016.11.004.
Menzel, W., Schreiner, W., 1977. Zum geomechanischen Verhalten von Steinsalz verschiedener Lagerstätten der DDR. Teil II: Das Verformungsverhalten. Neue Bergbautechnik 7 (8), 565–574.
Miranda, P.A.M.N., Vargas, E.A., Moraes, A., 2020. Evaluation of the Modified Cam Clay model in basin and petroleum system modeling (BPSM) loading conditions. Mar. Pet. Geol. 112 (November 2018), 104112 https://doi.org/10.1016/j.marpetgeo.2019.104112.
Nopola, J.R., Roberts, L.A., 2016. Time-dependent deformation of Pierre Shale as determined by long-duration creep tests. In: 50th US Rock Mechanics/Geomechanics Symposium, 584–591. https://onepetro.org/ARMAUSRMS/proceedings-abstract/ARMA16/All-ARMA16/ARMA-2016-508/126299.
Norton, F.H., 1929. Creep of Steel at High Temperatures. McGraw-Hill. https://archive.org/details/creepofsteelathi00nort/page/66/mode/2up?ref=ol&view=theater.
Perzyna, P., 1966. Fundamental problems in viscoplasticity. In: Advances in Applied Mechanics, pp. 243–377. Elsevier. https://doi.org/10.1016/s0065-2156(08)70009-7.
Rinaldi, A.P., Rutqvist, J., Luu, K., Blanco-Martín, L., Hu, M., Sentís, M.L., Eberle, L., Kaestli, P., 2022. TOUGH3-FLAC3D: a modeling approach for parallel computing of fluid flow and geomechanics. Comput. Geosci. https://doi.org/10.1007/s10596-022-10176-0.
Roscoe, K.H., Burland, J.B., 1968. On the Generalized Stress-Strain Behavior of 'Wet' Clay. Cambridge Univ Press.
Rutqvist, J., 2011. Status of the TOUGH-FLAC simulator and recent applications related to coupled fluid flow and crustal deformations. Comput. Geosci. 37 (6), 739–750. https://doi.org/10.1016/j.cageo.2010.08.006.
Rutqvist, J., 2020. Thermal management associated with geologic disposal of large spent nuclear fuel canisters in tunnels with thermally engineered backfill. Tunn. Undergr. Space Technol. 102 (April), 103454 https://doi.org/10.1016/j.tust.2020.103454.
Rutqvist, J., Börgesson, L., Chijimatsu, M., Hernelind, J., Jing, L., Kobayashi, A., Nguyen, S., 2009. Modeling of damage, permeability changes and pressure responses during excavation of the TSX tunnel in granitic rock at URL, Canada. Environ. Geol. 57 (6), 1263–1274. https://doi.org/10.1007/s00254-008-1515-6.
Rutqvist, J., Zheng, L., Chen, F., Liu, H.H., Birkholzer, J., 2014. Modeling of coupled thermo-hydro-mechanical processes with links to geochemistry associated with bentonite-backfilled repository tunnels in clay formations. Rock Mech. Rock Eng. 47 (1), 167–186. https://doi.org/10.1007/s00603-013-0375-x.
Rybacki, E., Herrmann, J., Wirth, R., Dresen, G., 2017. Creep of Posidonia Shale at elevated pressure and temperature. Rock Mech. Rock Eng. 50 (12), 3121–3140. https://doi.org/10.1007/s00603-017-1295-y.
Sasaki, T., Rutqvist, J., 2021. Estimation of stress and stress-induced permeability change in a geological nuclear waste repository in a thermo-hydrologically coupled simulation. Computers Geotechnics 129 (October 2020), 103866. https://doi.org/10.1016/j.compgeo.2020.103866.
Sasaki, T., Rutqvist, J., 2022. Effects of time-dependent deformation of shale on the integrity of a geological nuclear waste repository. Int. J. Rock Mech. Mining Sci. 158 (December 2021) https://doi.org/10.1016/j.ijrmms.2022.105206.
Schofield, A.N., Wroth, C.P., 1968. Critical State Soil Mechanics [University of Cambridge]. https://doi.org/10.1111/j.1475-2743.1987.tb00718.x.
Sone, H., Zoback, M.D., 2011. Visco-plastic properties of shale gas reservoir rocks. In: 45th US Rock Mechanics/Geomechanics Symposium. https://onepetro.org/ARMAUSRMS/proceedings-abstract/ARMA11/All-ARMA11/ARMA-11-417/120373.
Sone, H., & Zoback, M. (2013a). Mechanical properties of shale-gas reservoir rocks — Part 1: Static and dynamic elastic properties and anisotropy. *GEOPHYSICS*, *78*(5), D381–D392. https://doi.org/10.1190/geo2013-0050.1.
Sone, H., Zoback, M., 2013b. Mechanical properties of shale-gas reservoir rocks — Part 2: ductile creep, brittle strength, and their relation to the elastic modulus. Geophysics 78 (5), D393–D402. https://doi.org/10.1190/geo2013-0051.1.
Sone, H., Zoback, M.D., 2014. Time-dependent deformation of shale gas reservoir rocks and its long-term effect on the in situ state of stress. Int. J. Rock Mech. Min. Sci. 69, 120–132. https://doi.org/10.1016/j.ijrmms.2014.04.002.
Thomas, H.R., Vardon, P.J., Cleall, P.J., 2014. Three-dimensional behaviour of a prototype radioactive waste repository in fractured granitic rock. Can. Geotech. J. 51 (4), 246–259. https://doi.org/10.1139/cgj-2013-0094.
Tsang, C.F., Bernier, F., Davies, C., 2005. Geohydromechanical processes in the Excavation Damaged Zone in crystalline rock, rock salt, and indurated and plastic clays - In the context of radioactive waste disposal. Int. J. Rock Mech. Min. Sci. 42 (1), 109–125. https://doi.org/10.1016/j.ijrmms.2004.08.003.
Tsang, C.-F., 1987. Introduction to coupled processes. In: Tsang, C.-F. (Ed.), Coupled processes associated with nuclear waste repositories, pp. 1–6. Academic Press. https://www.elsevier.com/books/coupled-processes-associated-with-nuclear-waste-repositories/tsang/978-0-12-701620-7.
van Genuchten, M.T., 1980. A Closed-form Equation for Predicting the Hydraulic Conductivity of Unsaturated Soils1. In: Soil Science Society of America Journal, Vol. 44, Issue 5, p. 892. https://doi.org/10.2136/sssaj1980.03615995004400050002x.
Xu, H., Rutqvist, J., Plúa, C., Armand, G., Birkholzer, J., 2020. Modeling of thermal pressurization in tight claystone using sequential THM coupling: Benchmarking and validation against in-situ heating experiments in COx claystone. Tunn. Undergr. Space Technol. 103 (April), 103428 https://doi.org/10.1016/j.tust.2020.103428.
Yu, L., Weetjens, E., Sillen, X., Vietor, T., Li, X., Delage, P., Labiouse, V., Charlier, R., 2014. Consequences of the thermal transient on the evolution of the damaged zone around a repository for heat-emitting high-level radioactive waste in a clay formation: a performance assessment perspective. Rock Mech. Rock Eng. 47 (1), 3–19. https://doi.org/10.1007/s00603-013-0409-4.
Zhang, Q., Fink, R., Krooss, B., Jalali, M., Littke, R., 2021. Reduction of shale permeability by temperature-induced creep. SPE J. 26 (2), 750–764. https://doi.org/10.2118/204467-PA.